Table of Contents

1. EXECUTIVE SUMMARY

The project is composed of four phases total. The first three are towards in-plane, whereas the last one is towards out-of-plane displacement/distance sensing. In the first two phases, PHASE 1 and PHASE 2, normally-off and in the third phase normally-on sensors are investigated. While PHASE 1 focuses on large-range low-sensitivity sensors, PHASE 2 focuses on short-range high-sensitivity ones. This Periodic Report mentions numerous sensor designs obtained within the concept of the Project Proposal named "*NANO-DISP: Theoretical and Experimental Investigation of Synchronous Silicon Nanowire Waveguide Displacement Sensors*" towards large-range low-sensitivity and short-range high-sensitivity measurement characteristics as promised in PHASE 1 and PHASE 2, respectively, in the first two years. 3D Finite-Difference Time-Domain (FDTD) Analysis is utilized in the efforts towards numerical characterization of the sensors. PHASE 1 involved a single type of sensing mechanism, whereas in PHASE 2, two types of mechanisms are considered. Sensors in PHASE 1 are based on waveguide tips with elliptical geometry. Results demonstrated that the angle and length of tip geometry affect optical characteristics of the sensors under consideration. Among all suitable sensors, the highest sensitivity per percent of light intensity is calculated to be 5.74 nm at 80º tip angle for 4.8 μm tip length and 1.5 μm tip width, and the lowest sensitivity is calculated to be 9.62 nm at 85º tip angle for 12.0 μm tip length and 1.5 μm tip width. The smallest and largest measurement ranges achievable are foreseen to be 674 nm and 1062 nm, respectively.

First type of the sensors studied in PHASE 2 is based on waveguide tips with elliptical geometry similar to those in PHASE 1. The novelty for this type, however, is the use of tip angles below the Brewster's. Among all appropriate sensors in this type are those with 4.8 μm tip length and 1.5 μm tip width. The highest sensitivity is 1.10 nm per percent of light intensity at 10º tip angle, and the lowest sensitivity is 5.74 nm per percent of light intensity at 50º tip angle. The smallest and largest measurement ranges achievable based on calculations are predicted to be 135 nm and 674 nm, respectively. Second type of the sensors investigated in PHASE 2 is composed of two identical waveguides with tapered tips with abrupt ends. Studies proved that tip width, tip-end size, tip angle and thickness affect optical characteristics. Numerical studies on TYPE 2 sensors are still on the way for optimal solution, however, so far the highest sensitivity per percent of light intensity is calculated to be 0.97 nm at 9.5º tip angle for 100 nm tip-end size, 300 nm thickness and 600 nm tip width, and the lowest sensitivity is calculated to be 3.40 nm at 10.5º tip angle for 200 nm tip-end size, 170 nm thickness and 600 nm tip width. The smallest and largest measurement ranges achievable are calculated to be 97 nm and 330 nm, respectively.

In PHASE 3, short-range high-sensitivity in-plane displacement sensors again, but at normally-on state are being investigated in order to clarify their initial state effects on the sensing characteristics. Towards this goal, three major types of sensor approaches are studied. All sensors utilized in PHASE 3 are based on Electromagnetic Field Modulation (EFM). Sensitivities achieved in this phase are from 0.84 nm down to 0.06 nm per percent of light intensity within sub-100 nm distances.

Among major milestones succeeded in the project so far, procurement of two and three dimensional design and file conversion software for use in sensor design process, and FDTD Analysis software and the workstations for numerical studies can be counted. In addition, Micro/Nano Research Centers suitable for successful fabrication of the promised sensors are contacted and agreed. Fabrication of the sensor devices is being carried out at the agreed cleanroom of Bilkent University, Ankara, Turkey's *National Nanotechnology Research Center* (*UNAM,* http://www.nano.org.tr/). Graduate student researchers are hired, educated

and trained, and micro/nano-fabrication recipes are clarified after significant number of iterations. Several interesting sensors characterized numerically as mentioned above are fabricated in order to obtain their mechanical and optical characteristics experimentally for verification. Sensor cores where the actual measurement takes place are only 50зm × 80зm in size. The project workpackages are accomplished mostly in the so-called *Nanophotonic Systems Research Laboratory* (*NANOPSYS*) at Ozyegin University, Istanbul, Turkey and the very small portion of the rest very recently at Istanbul Technical University (ITU), Istanbul, Turkey. *NANOPSYS* currently involves three graduate and two undergraduate students as well as the Principal Investigator (PI). Design and fabrication of home-made Vapor HF Etching Setup for Device Release is realized with the help of the undergraduate students. Finally, fund search for procurement of both Mechanical and Optical Sensor Characterization Setups, and their installation are completed. When compared to the project's workplan promised in the proposal, owing to the duration it took to grant the support for the procurement of characterization setups from a subsequent funding agency, *the Scientific and Technological Research Council of Turkey* (*TUBITAK*, http://www.tubitak.gov.tr/en/ot/10/), in addition to EC FP7 Marie Curie IRG Programme's Support, the project is delayed approximately by four to six months from the experimental point of view. However, the grant needed for the characterization setups are ensured properly, and as a result, currently, both mechanical and optical characterization of the sensors promised at PHASE 1 are very close to the end, predicted to be completed in about a month. Because of the delay in granting subsequent funding, it hasn't been possible for the research group to fulfill and include the experimental characterization results into this Periodic Report at hand unfortunately. Nevertheless, in order to make the delay up and to ensure completion of the promised workpackages fully in the rest of the project's total duration of four years, the research group had already gone ahead to the second phase, PHASE 2, and third phase, PHASE 3, and completed more than that planned in terms of numerical analysis and design. As a result, we anticipate that all workpackages will be fulfilled prior to the end of the project term successfully. Despite difficulties encountered, PI has succeeded to reach the critical mass within the European Union in financial, infrastructural and researcher aspects in order to ensure microfabrication and characterization of high-sensitivity embedded optical displacement/distance sensors.

2. PHASE 1

2.1. Normally-off Large-range Low-sensitivity Physical Contact Displacement Sensors

For the success of following phases promised, fabrication and characterization of normally-off large-range low-sensitivity silicon subwavelength-scale waveguide in–plane displacement sensor using the outcomes of [1] is targeted to be realized to implement microfabrication techniques in a standard manner within the host organization.

2.1.1. Sensor Structure and Principle

The proposed normally-off large-range low-sensitivity displacement sensors consist of subwavelength-scale silicon input and output waveguides, and a moving waveguide rigidly connected to the source of the motion, which in this project is imitated by an embedded electrostatic comb actuator, as shown schematically in Fig. 1. The equivalent spring coefficient is calculated to be 0.52/m. Each finger of the comb actuator is 2 μm long and 200 nm wide. Initial finger overlap is 300 nm. Gap between finger pairs is 300 nm.

At the beginning, the moving waveguide is offset by the air gap from the input and output waveguides. When a voltage is applied to the actuator, moving waveguide closes the air gap. Physical contact or proximity of waveguide tips enables greater light propagation from the input to the output through the moving waveguide with respect to the beginning state. Change in the transmitted light intensity through the moving waveguide as a function of proximity distance forms the fundamental concept of the sensing mechanism.
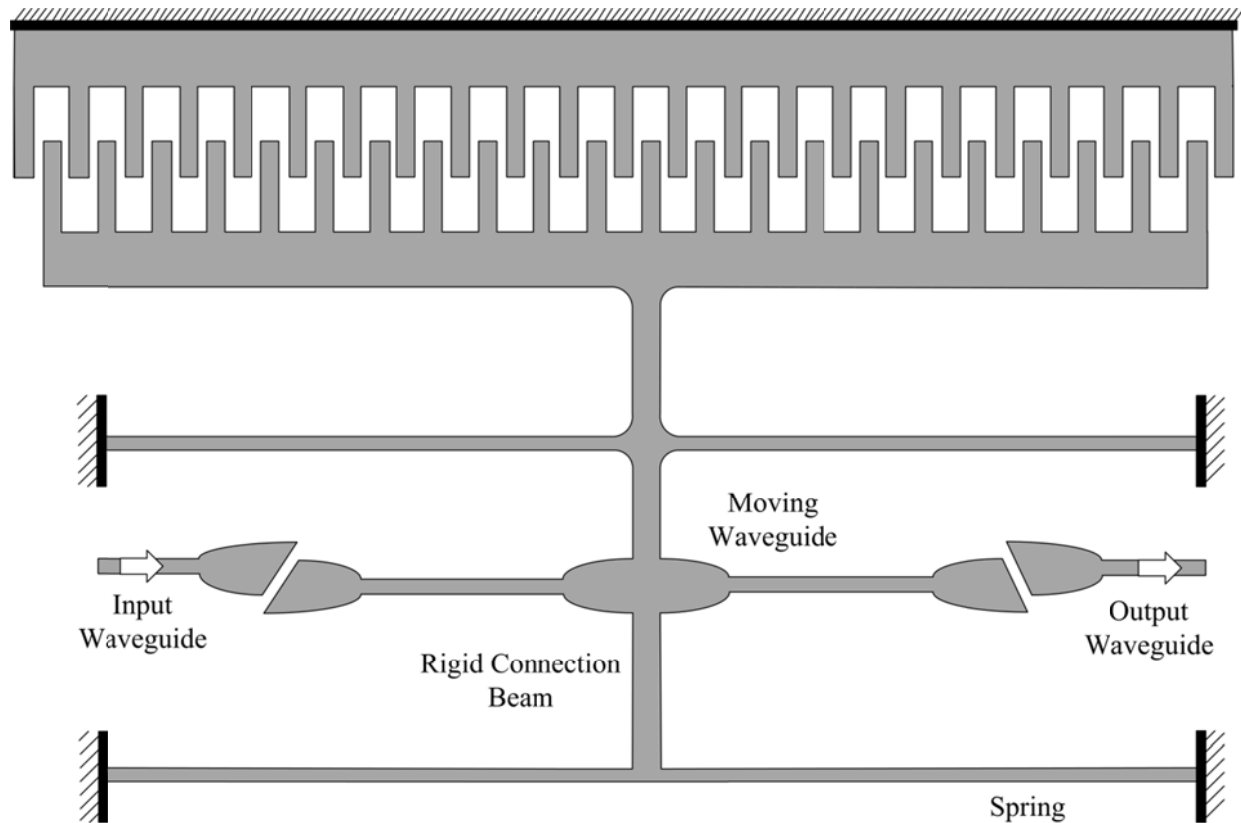

Figure 1: *Schematic illustration of the displacement sensor.*

2.1.2. Numerical Study in FDTD

Displacement sensor simulations are numerically conducted in 3D Finite-Difference Time-Domain (FDTD) Analysis software, namely FullWAVE of RSoft Inc. Refractive indices of silicon, SiO_2, and air are 3.46, 1.47, and **1**, respectively. For single-mode TE-polarized light at 1.55 μm wavelength, waveguide width and thickness are 500 nm and 260 nm, respectively. Incident TE polarized electric field is perpendicular to the device layer. Thickness of SiO_2 must at least be 1 μm in order to keep optical propagation loss in the waveguides less than 0.001 dB/cm [2]. SiO_2 as the bottom cladding is designed as 2 μm and upper cladding is air material. The grid size is selected to be 25 nm, since, for reliable calculation, it must be smaller than one tenth of the smallest dimension in the model.

2.1.2.1. Effects of Relative Waveguide Positions and Tip Angle

Elliptical tip geometry, which is 1.5μm-wide, 7.2μm-long, and 260nm-thick, is designed to facilitate the physical contact of waveguides to maximize optical transmission and contrast, thereby, increasing the measurement sensitivity to acceptable levels. Figure 2 illustrates two possible relative waveguide positions for a waveguide tip pair designed and simulated. Both design have the tip angle of θ. While the first as in Fig. 2a, a distance perpendicular to light propagation direction, D, in Fig. 2b, a distance along the propagation direction, L, is left.
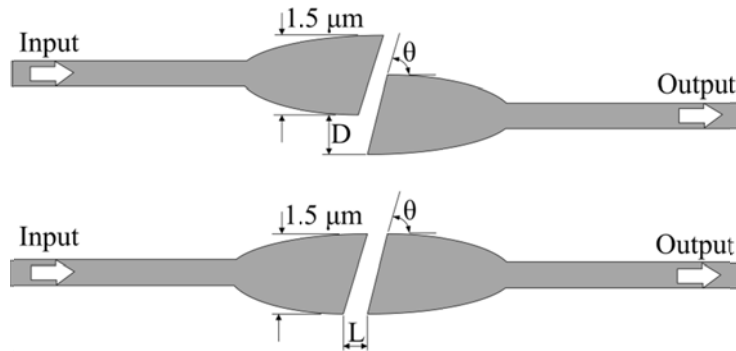

Figure 2: *Two possible relative waveguide positions. a) Perpendicular to light propagation direction, b) Along the propagation direction.*

The relations between Brewster's angle, θ_B, angle of incidence, θ_1, angle of refraction, θ_2, refractive index of air, n_1, refractive index of silicon n_2 are given in equations (1), (2) and (3). When incident angle, θ_1, is equal to the Brewster's angle, θ_B, no light gets back-reflected. From the Snell's Law, critical angle for silicon/air pair is approximately 16.3°. Brewster's angle is the complement of critical angle, which corresponds to 73.7° for silicon/air pair. In this phase, three tips with an angle above the Brewster's and two below are investigated in order to understand the effect of tip angle in the elliptical geometry. To be specific, tip angles of 65°, 70°, 74°, 80°, and 85° are simulated.

$$\theta_1 + \theta_2 = 90° \quad\text{...} \quad (1)$$

$$n_1 . \sin \theta_1 = n_2 . \sin \theta_2 \quad\text{...} \quad (2)$$

$$\theta_B = arc\ tan(\frac{n_2}{n_1}) \quad\text{...} \quad (3)$$

First, optical performance of structures shown in Fig. 2a is studied at 100 nm, 200 nm, 400 nm, and 600 nm distances. Figure 3 depicts typical cases where the behavior of the lightwave and, hence, optical performance changes. As seen in Fig. 3a, transmittance is 91.31% at a tip angle of 74° when the distance between the waveguides is zero. When the distance for the same geometry is increased to 600 nm, transmittance decreases down to 11.12% as illustrated in Fig. 3b. Transmittance with tip angles above the Brewster's is observed to be greater. At a distance of 100 nm at 74° tip angle, transmittance increases to 97.31% as it can be seen in Fig. 3c. Transmittance calculated at 100 nm distance is greater than that at 0 nm, because the tip satisfies the Brewster's angle. However, for tip angles below the Brewster's angle, yields high loss as in the tip with 65° even at 100 nm distance as shown in Fig. 3d.
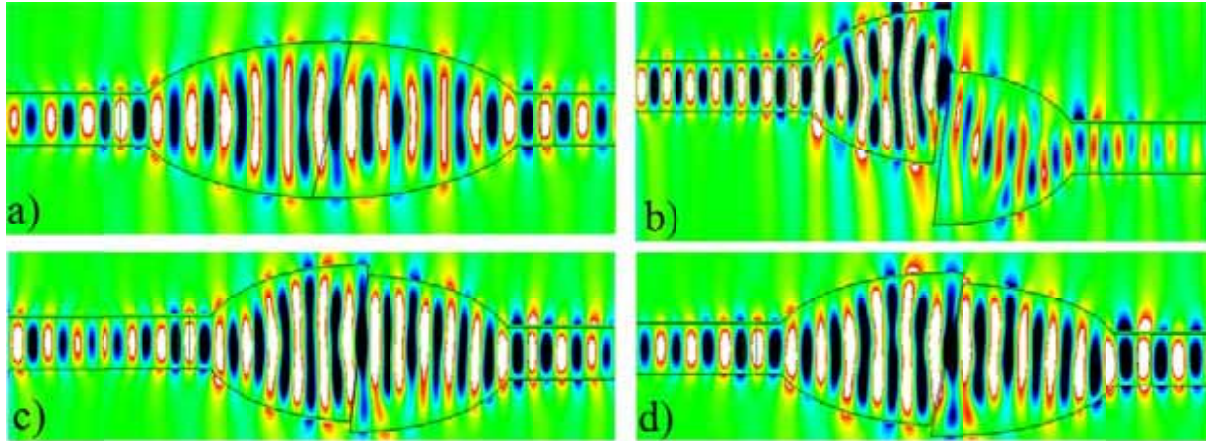

Figure 3: *Electric field (E_x) of the lightwave as a function of distances for various tip angles. a) At 0 nm at 74°, b) at 600 nm at 74°, c) at 100 nm at 74°, d) at 100 nm at 65°.*

Figure 4 shows the complete set of results obtained including those presented in Fig. 3 in the numerical study. It is understood that the larger tip angle, the higher transmittance. 85° tip angle, for example, is suitable for large-range displacement sensors because transmittances are high above 90% at both 0 nm and 200 nm distances, and also because transmittance is still high about 35% at even 600 nm, offering even larger distances for measurement. 65° tip angle, on the other hand, seems to be useful for short-range high-sensitivity sensors rather than large-range low-sensitivity ones due to sudden decline between 0 nm and 300 nm distances. Hence, tip angles above the Brewster's such as 74°, 80° and 85° seem to be suitable as normally-off large-range low-sensitivity sensors. When micro/nano-fabrication constraints are considered, tip angles above the Brewster's and below approximately 80° are expected to be the most appropriate.
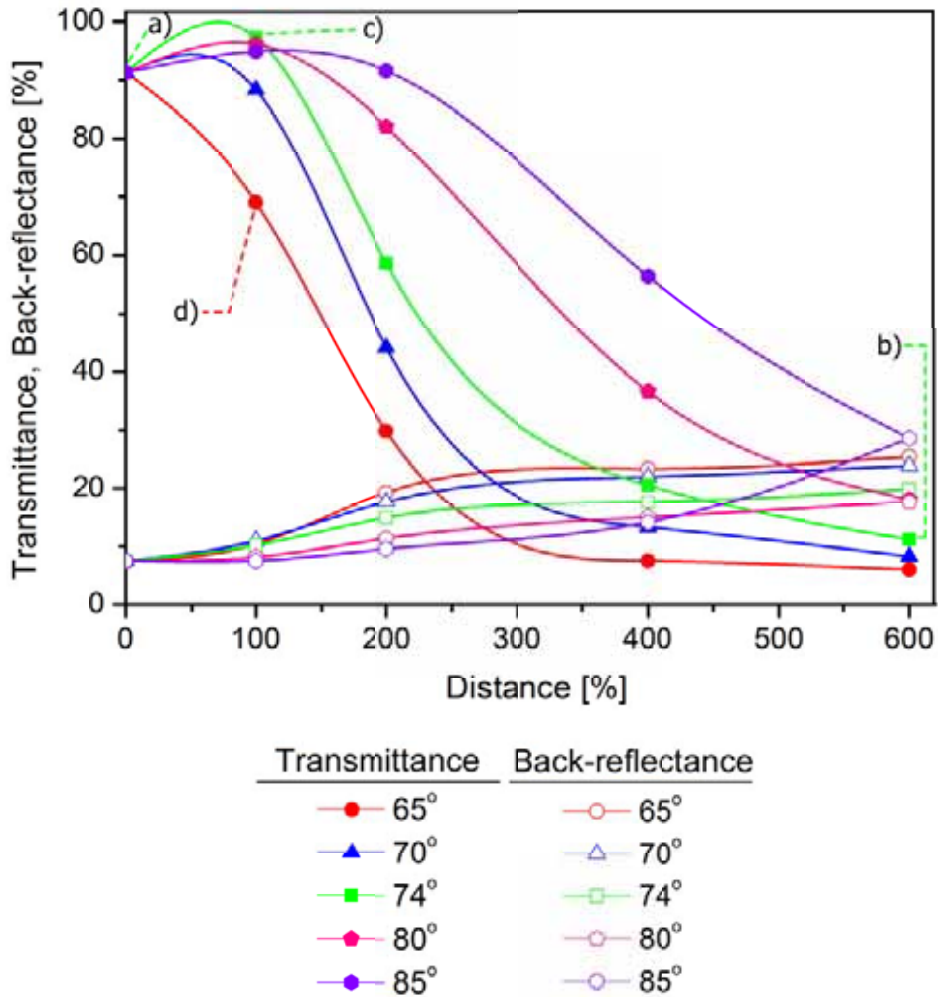
Figure 4: *Simulated transmittance and back-reflectance as a function of distance, D, at the tip angles, θ, of 65°, 70°, 74°, 80°, and 85°.*

Optical performance of structures as illustrated in Fig. 2b are studied at 100 nm, 200 nm, 400 nm, and 600 nm distances, results of which are given in Fig. 5. Results again point that the smaller the tip angle, the smaller the transmittance. Results of the study also indicate that regardless the tip angle is above or below the Brewster's, the sensor will be highly prone to fabrication errors within sub-100 nm distances, where surface roughnesses also fall into, owing to significant loss calculated numerically. Thus, measurement sensitivities from 0 nm to 100 nm will be far below acceptable levels. Hence, sensor structures positioned as in Fig. 2b cannot be utilized in realization of large-range low-sensitivity measurements.
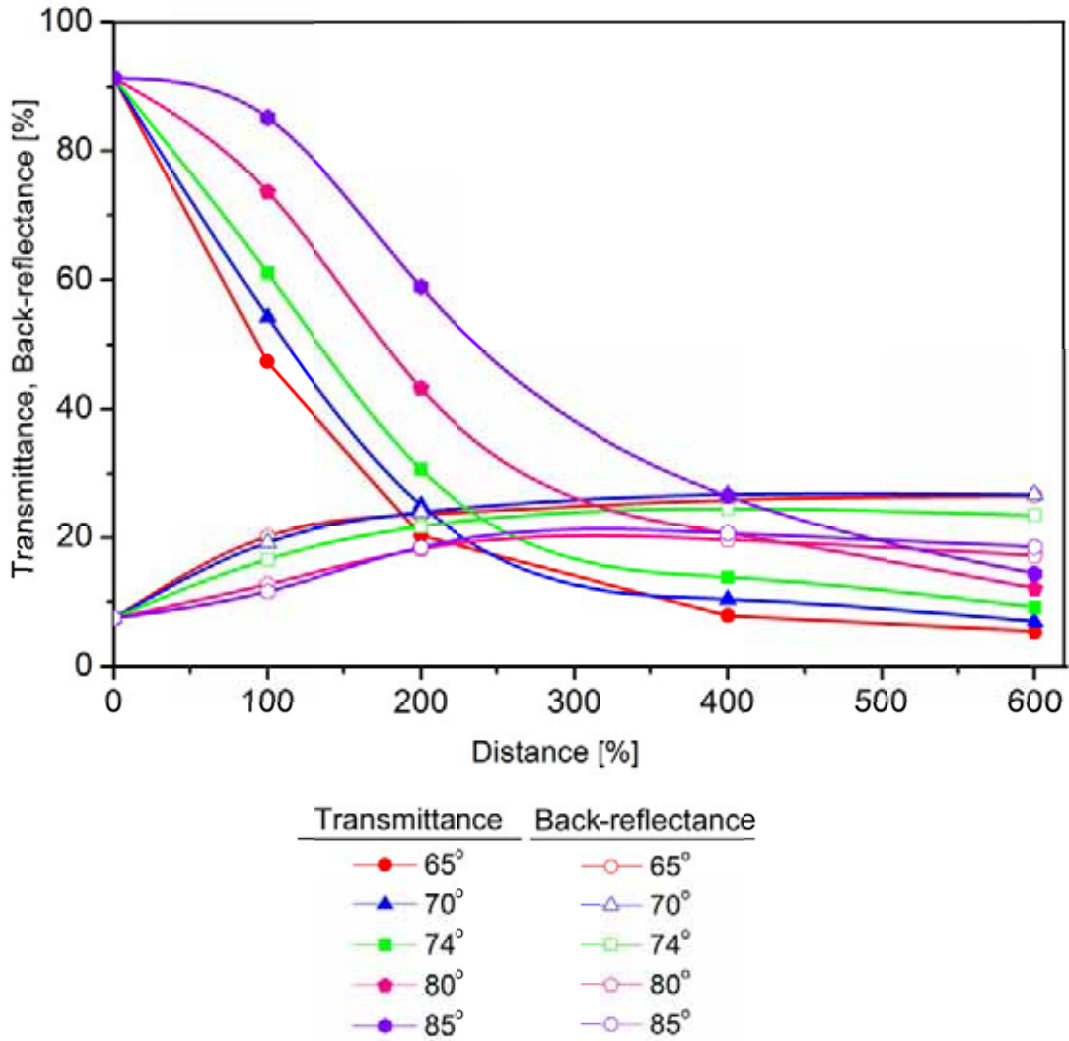
Figure 5: *Simulated transmittance and back-reflectance as a function of distance, L, at the tip angles, θ, of 65º, 70º, 74º, 80º, and 85º.*

2.1.2.2. Effect of Elliptical Tip Geometry Length

After the effects of relative waveguide positions and tip angle on optical character is understood, elliptical tip geometries with different lengths are investigated. The aforementioned studies employed a length of 7.2 μm in the elliptical geometry. Below elliptical tip geometries with lengths of 4.8 μm, 6.0 μm, 8.4 μm, 9.6 μm, 10.8 μm and 12.0 μm are conducted to figure out their effect. Results are as discussed below.

Transmittance and back-reflectance as a function of distance, D, at the tip angles, θ, of 65º, 70º, 74º, 80º, and 85º for 4.8 μm length and 1.5 μm width of elliptical geometry at 100 nm, 200 nm, 400 nm, and 600 nm distances are simulated. Results are given in Fig. 6.

As it will be mentioned in the following parts of this report in the details of the sensor fabrication process, in the worst case, a maximum of 100 nm air gap (distance) can be achieved on the physically-contacting sidewalls of sensor tip geometries due to the microfabrication limits. The highest transmittance will be seen at this small distance within 100 nm, where the possible highest contrast in transmittance will be attained for large-range sensors. Hence, elliptical geometries with 74º and 80º tip angles are the best candidates towards realization of large-range low-sensitivity sensors. The contrast values for these elliptical geometries are calculated to be 84.64% and 86.96% causing measurement ranges of 690 nm and 674 nm, respectively. Optical performances at the aforementioned geometries change from 88.37% to 3.7% and from 94.43% to 12.46% at 100 nm and 600 nm displacement values, corresponding to sensitivities of about 5.90 nm and 5.74 nm per percent of light intensity, again respectively.
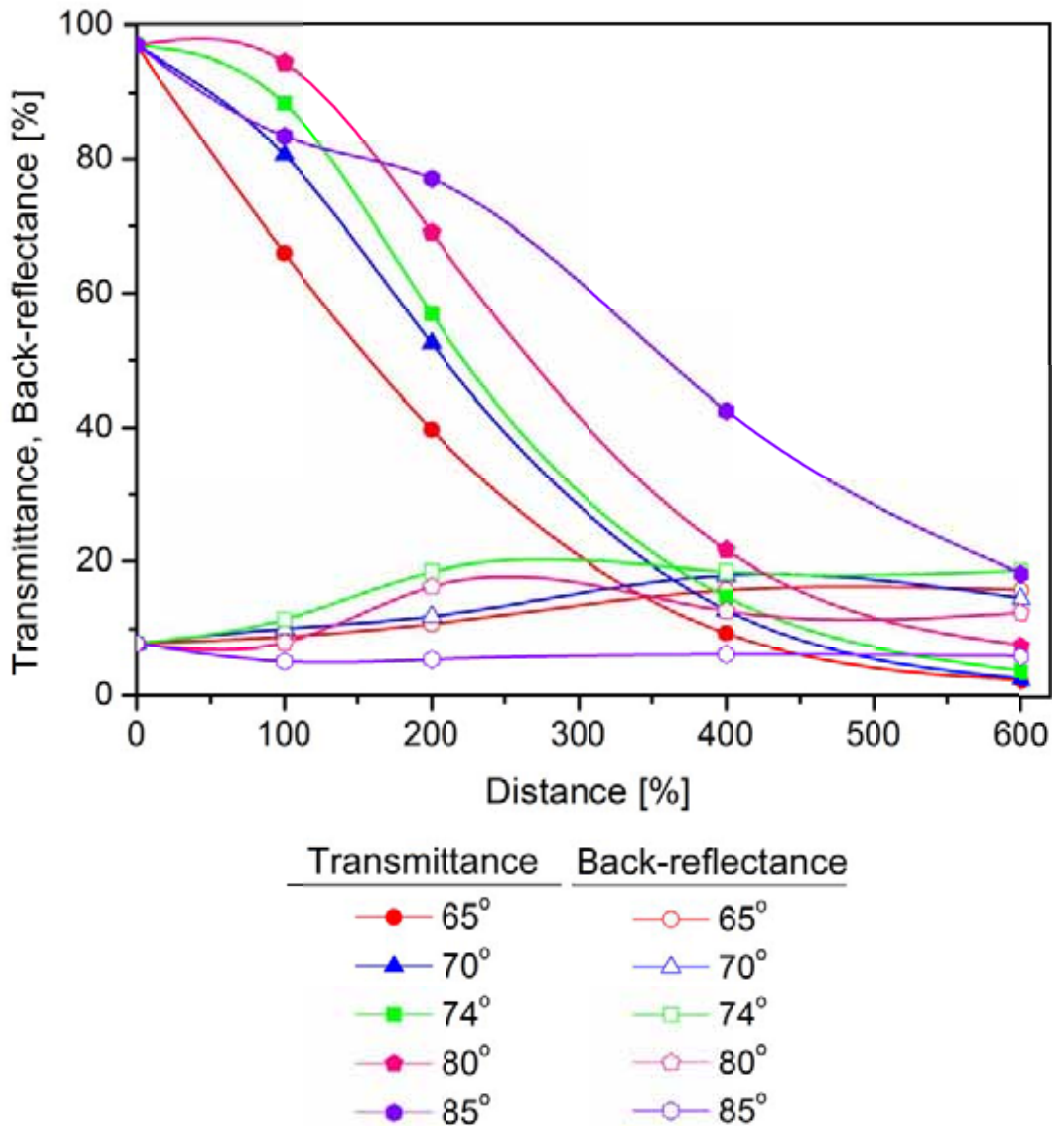

Figure 6: *Calculated transmittance and back-reflectance as a function of distance, D, at the tip angles, θ, of 65º, 70º, 74º, 80º, and 85º for 4.8 µm length of elliptical geometry.*

Next, transmittance and back-reflectance as a function of distance, D, at the tip angles, θ, of 65º, 70º, 74º, 80º, and 85º as studied for 4.8 μm, but this time for 6.0 μm length and 1.5 μm width of elliptical geometry at 100 nm, 200 nm, 400 nm, and 600 nm distances are numerically studied. Results are given in Fig. 7. At this step, change in contrast caused by fabrication errors for elliptical sensor geometries with 74º, 80º, and 85º tip angles will be useful. The contrast values for these elliptical geometries are calculated to be 76.29%, 70.52% and 58.15% causing measurement ranges of 755 nm, 809 nm and 959 nm, respectively. Optical performances at the aforementioned geometries change from 81.29% to 5.00%, from 84.69% to 14.17%, and from 85.23% to 27.08% at 100 nm and 600 nm displacement values, corresponding to sensitivities of about 6.55 nm, 7.09 nm, and 8.59 nm per percent of light intensity, respectively.
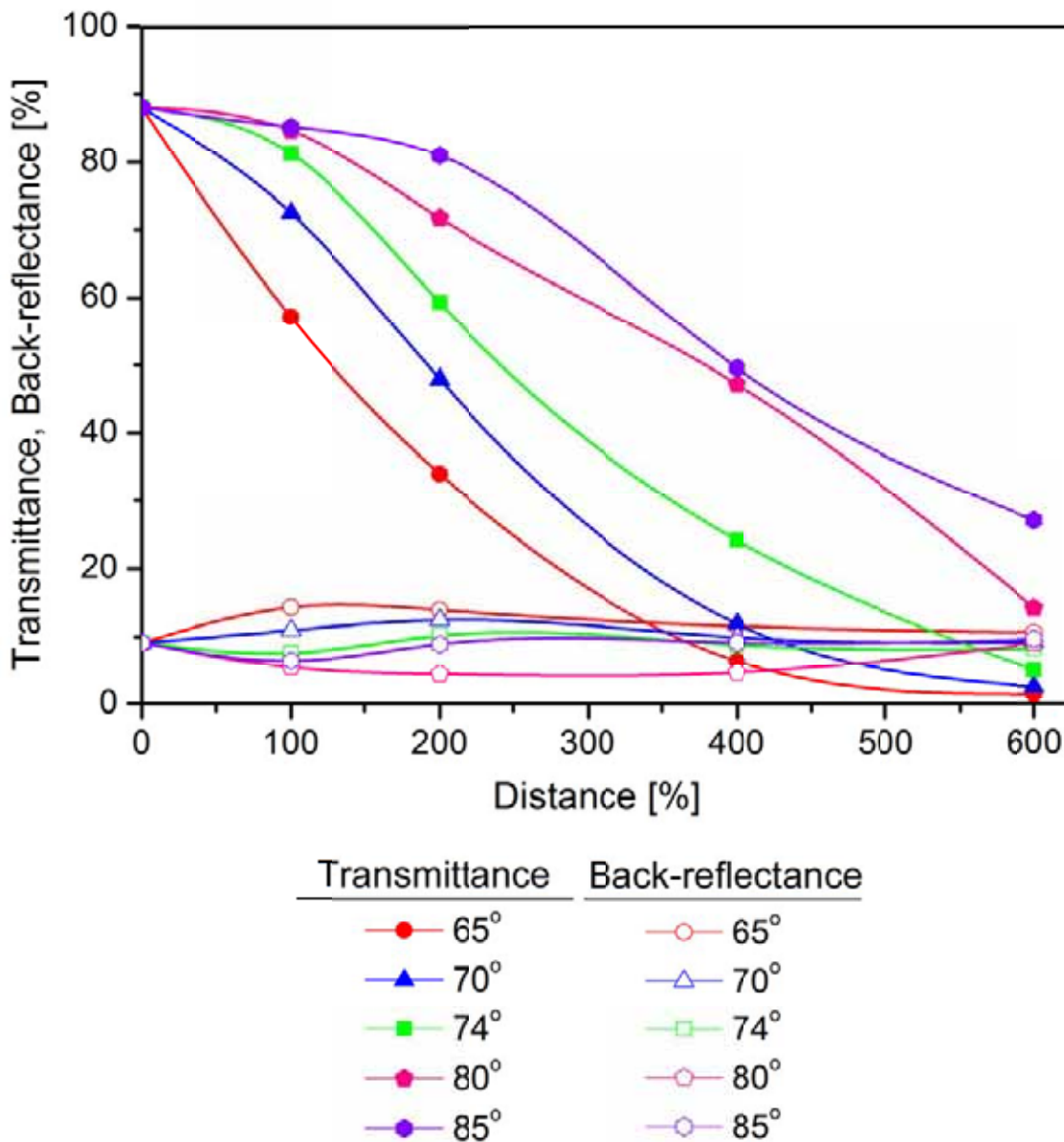

Figure 7: *Calculated transmittance and back-reflectance as a function of distance, D, at the tip angles, θ, of 65º, 70º, 74º, 80º, and 85º for 6.0 μm length of elliptical geometry.*

Later, transmittance and back-reflectance again for the same elliptical geometry, but with a length of 8.4 µm are numerically calculated. Results are given in Fig. 8. 8.4 µm is understood to be the most appropriate length for large-range displacement sensors because not only high contrast values at all studied tip angles of 65º, 70º, 74º, 80º, and 85º are achieved, but also highest contrast values when compared to results of other studied elliptical geometry lengths are obtained. Measurement ranges of respective 722 nm, 732 nm, 799 nm, 911 nm, and 1017 nm are observed. FDTD analysis showed that the studied elliptical geometries yielded corresponding sensitivities of about 6. 22 nm, 6.32 nm, 6.99 nm, 8.11 nm, and 9.17 nm per percent of light intensity.
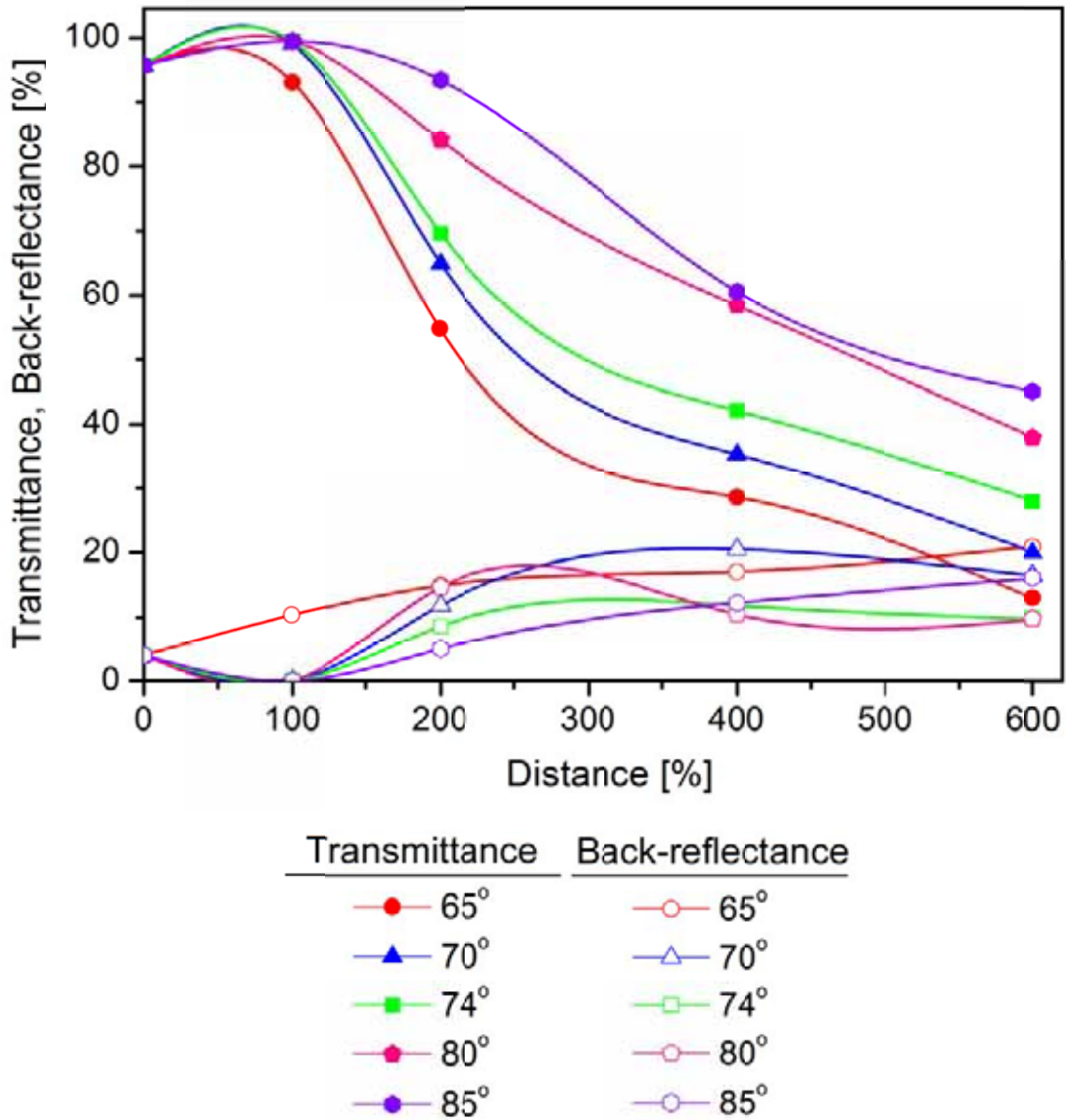

Figure 8: *Calculated transmittance and back-reflectance as a function of distance, D, at the tip angles, θ, of 65º, 70º, 74º, 80º, and 85º for 8.4 µm length of elliptical geometry.*

Next, transmittance and back-reflectance for the same elliptical geometry, but with a length of 9.6 μm are studied. Results are given in Fig. 9. Contrasts in transmittance for sensors with 65°, 70°, and 74° tip angles at 100 nm and 600 nm are appropriate in large-range measurements. Respective measurement sensitivities are calculated to be 6.90 nm, 8.20 nm, and 8.02 nm per percent of light intensity. Sensors with 80° and 85° tip angles are understood to be suitable in measurements in the range from 200 nm to 600 nm, suggesting non-contact large-range sensors eliminating fabrication errors by nature. Numerically analysis in the latter case showed that the studied elliptical geometries yielded corresponding sensitivities of about 6.76 nm and 9.06 nm per percent of light intensity.
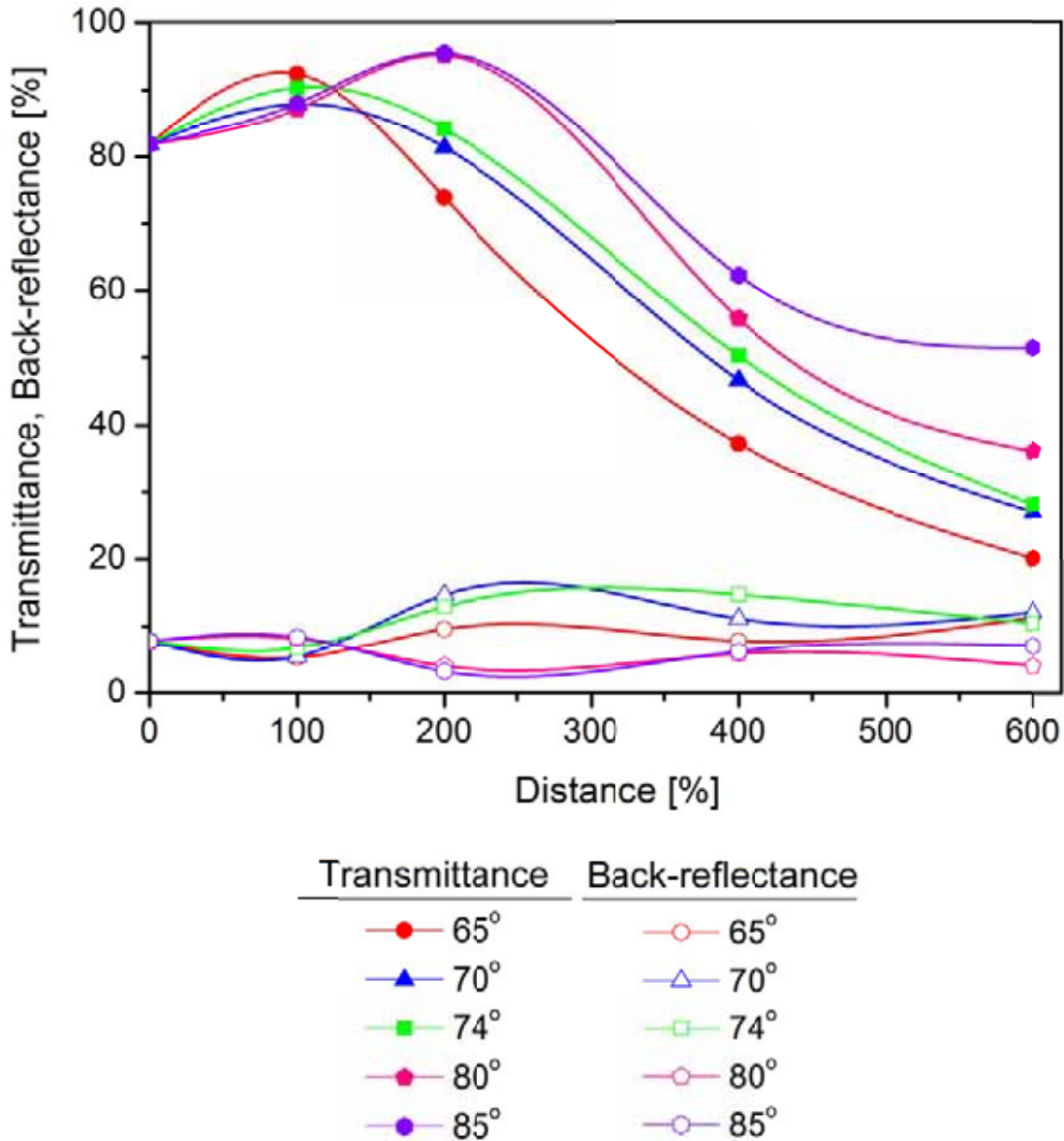

Figure 9: *Calculated transmittance and back-reflectance as a function of distance, D, at the tip angles, θ, of 65°, 70°, 74°, 80°, and 85° for 9.6 μm length of elliptical geometry.*

Next, transmittance and back-reflectance for the same elliptical geometry, but with a length of 10.8 μm are studied. Results are given in Fig. 10. Elliptical geometries with 65º, 70º, and 74º tip angles are obtained to be suitable for short-range sensors owing to their rapid decrease from 0 nm to 600 nm distances range. Those with 80º and 85º tip angles, on the other hand, are appropriate for large-range low-sensitivity displacement sensors, yielding transmittance contrasts of 74.47% and 70.62% causing measurement ranges of 771 nm and 808 nm, respectively. Optical performances change from 92.44% to 17.97% and from 92.49% to 21.87% at 100 nm and 600 nm displacement values, corresponding to sensitivities of about 6.71 nm and 7.08 nm per percent of light intensity.
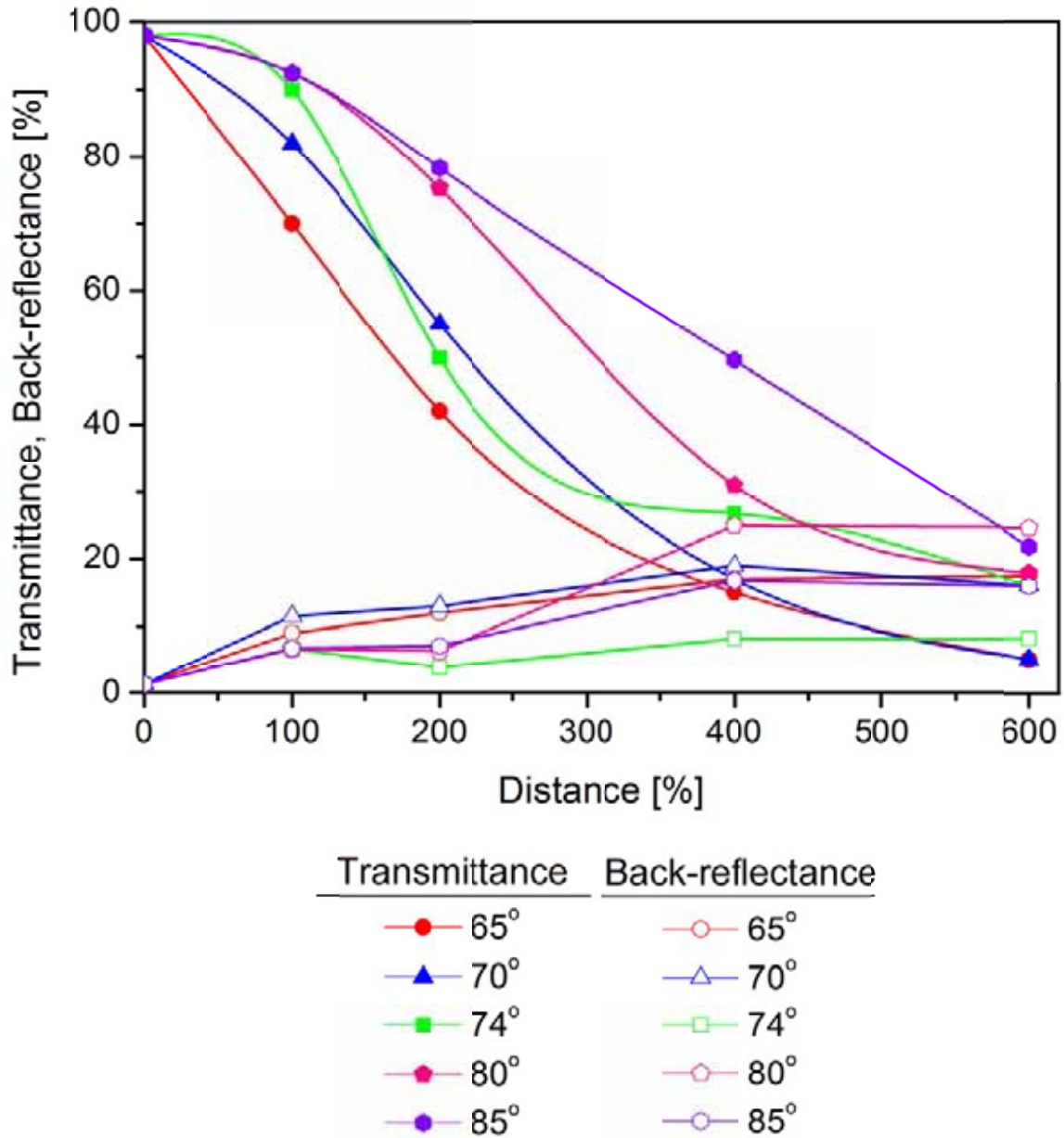

Figure 10: *Calculated transmittance and back-reflectance as a function of distance, D, at the tip angles, θ, of 65º, 70º, 74º, 80º, and 85º for 10.8 μm length of elliptical geometry.*

Last, transmittance and back-reflectance for the elliptical geometry with a length of 12.0 μm are calculated. Results are given in Fig. 11. Contrasts in transmittance for sensors with 80º and 85º tip angles at 100 nm and 600 nm are appropriate in large-range measurements. The contrast values for these elliptical geometries are calculated to be 63.81% and 51.97% causing measurement ranges of 883 nm and 1062 nm, respectively. Numerically study showed that the elliptical geometries yielded respective sensitivities of about 7.83 nm and 9.62 nm per percent of light intensity.
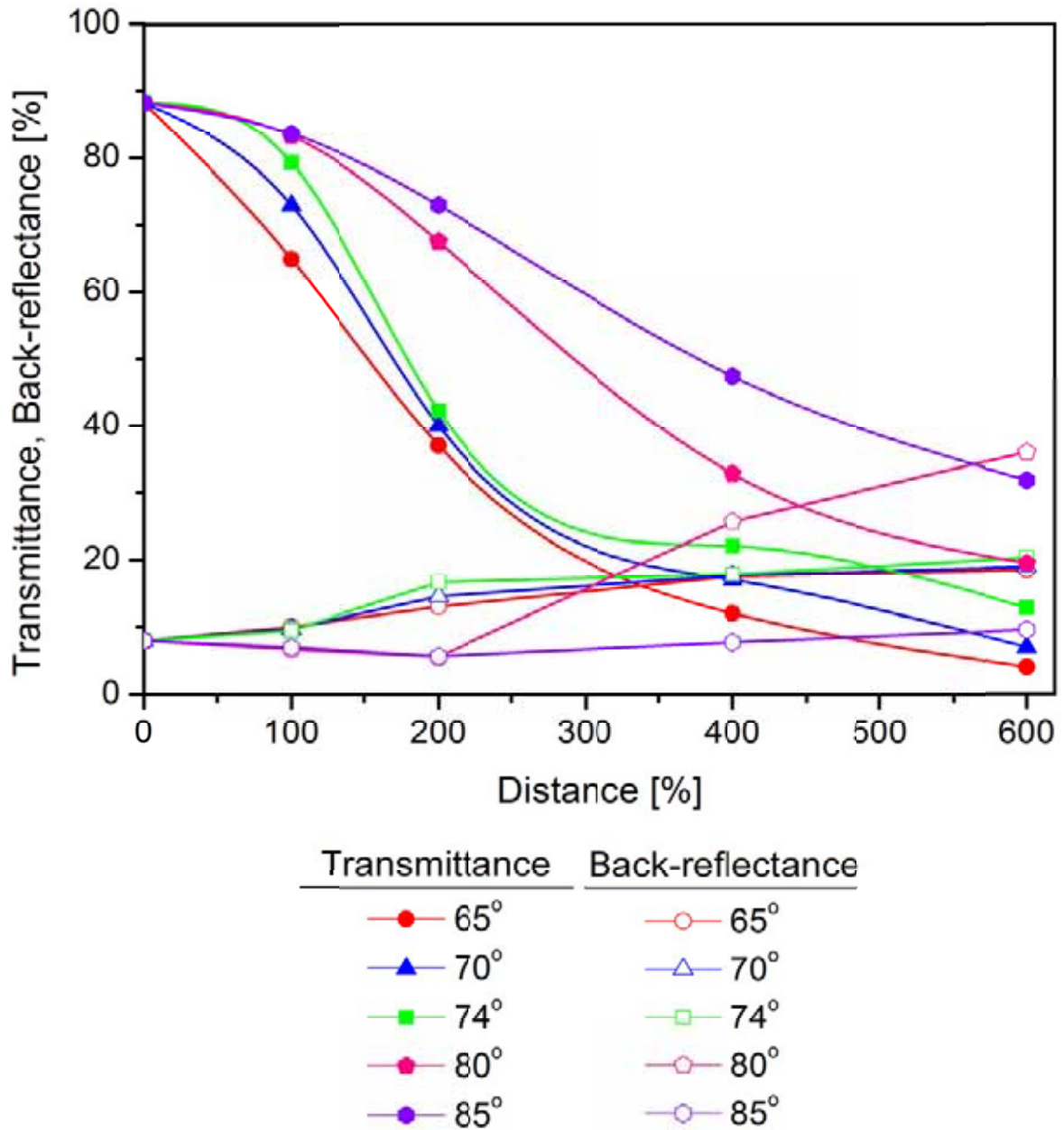

Figure 11: *Calculated transmittance and back-reflectance as a function of distance, D, at the tip angles, θ, of 65º, 70º, 74º, 80º, and 85º for 12.0 μm length of elliptical geometry.*

Numerous models suitable for large-range low-sensitivity sensors are obtained. Studies demonstrated that length of elliptical tip geometry affects optical characteristics. In all tip lengths, higher contrasts in transmittance are achieved for tip angles above the Brewster's, whereas smaller values are observed in smaller tip angles than the Brewster's for the same length. In this phase, 22 different sensor designs are learned to be suitable for realization of the large-range displacement sensors. For a tip length of 4.8 µm, tip angles of 74º and 80º, for 6.0 µm, 74º, 80º and 85º, for 7.2 µm, 74º, 80º and 85º, for 8.4 µm, 65º, 70º 74º, 80º and 85º, for 9.6 µm, 65º, 70º 74º, 80º and 85º, for 10.8 µm, 80º and 85º, and for 12.0 µm, 80º and 85º are understood to be appropriate. Among all suitable sensors, the highest sensitivity per percent of light intensity is calculated to be 5.74 nm at 80º tip angle for 4.8 µm tip length and 1.5 µm tip width, and the lowest sensitivity is calculated to be 9.62 nm at 85º tip angle for 12 µm tip length and 1.5 µm tip width. Hence, the smallest and largest measurement ranges achievable are foreseen to be 674 nm and 1062 nm, respectively.

2.1.3. Design of Actuator as the Source of Motion

Actuators as the source of motion can be embedded in order to experimentally verify optical characteristics of sensors as a function of distance. Electrostatic comb-drive actuation is a common mechanism in microelectromechanical systems (MEMS) [3]. Such comb-drives can be actuated in in-plane or out-of plane modes. In the sensors under consideration, in-plane actuation mode will be utilized. Figure 12 depicts the schematic view of integrated sensor-actuator design in mind.
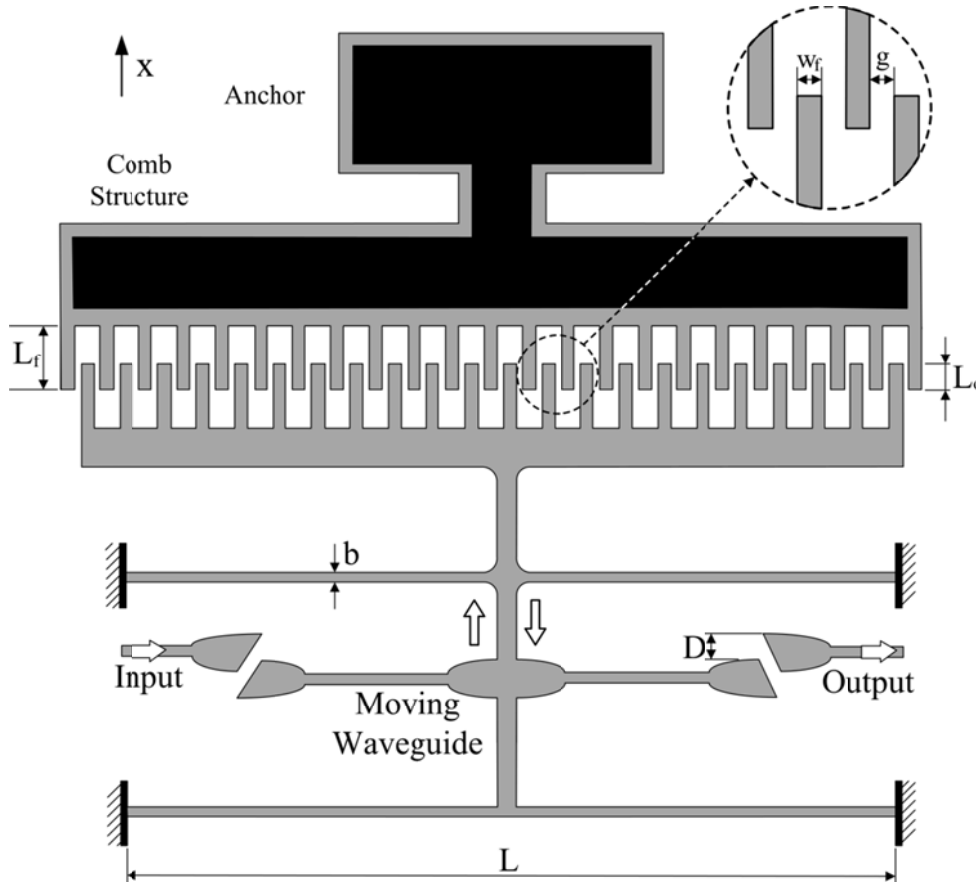
Figure 12: *Schematic diagram of electrostatic comb-drive actuator.*

In this particular design, total electrostatic force, F_x, moment of inertia, I_x, maximum stable deflection, δ_x, spring coefficient, K_x, all along x direction are as given in equations (4), (5), (6) and (7) below.

$$F_x = \frac{n.\varepsilon.t.V^2}{2g} \quad \text{...} \quad (4)$$

$$I_x = \frac{b.t^3}{12} \quad \text{...} \quad (5)$$

$$\delta_x = \frac{n.\varepsilon.V^2.L^3}{16.E.g.b^3} \quad \text{...} \quad (6)$$

$$K_x = \frac{2.E.h.b^3}{l^3} \quad \text{...} \quad (7)$$

In this particular design, n is the number of finger pairs in the comb actuator, g is the gap between stationary and moving comb finger pairs, w_f is finger width, t is finger thickness, L_f is finger length, L_0 is initial finger overlap, b is spring beam width, h is spring beam thickness, L is spring beam length, E is Young's Modulus for single crystalline silicon, ε is permittivity of air, and V is applied DC bias voltage. Values of the parameters listed above are provided in Table 1.

Table 1. Specification of the comb-drive actuator.

Symbol	Name	Value
n	Finger Pairs	37
g	Finger Spacing	0.30 μm
w_f	Finger Width	0.20 μm
t	Finger Thickness	0.26 μm
L_f	Finger Length	2.00 μm
L_o	Finger Overlap	0.30 μm
b	Spring Width	0.25 μm
h	Spring Thickness	0.26 μm
L	Spring Length	35.88 μm
E	Young's Modulus	185 GPa
ε	Permittivity	1.885E-4
V	Bias Voltage	0-55.8 V

In order to achieve 1.7 μm displacement range, D, at approximately 55.8 V DC for covering any possible distance under investigation of sensors, a set of two double-clamped flexures with an equivalent spring coefficient of 0.52 N/m is designed. The calculated distance versus bias voltage curve is depicted in Fig. 13.
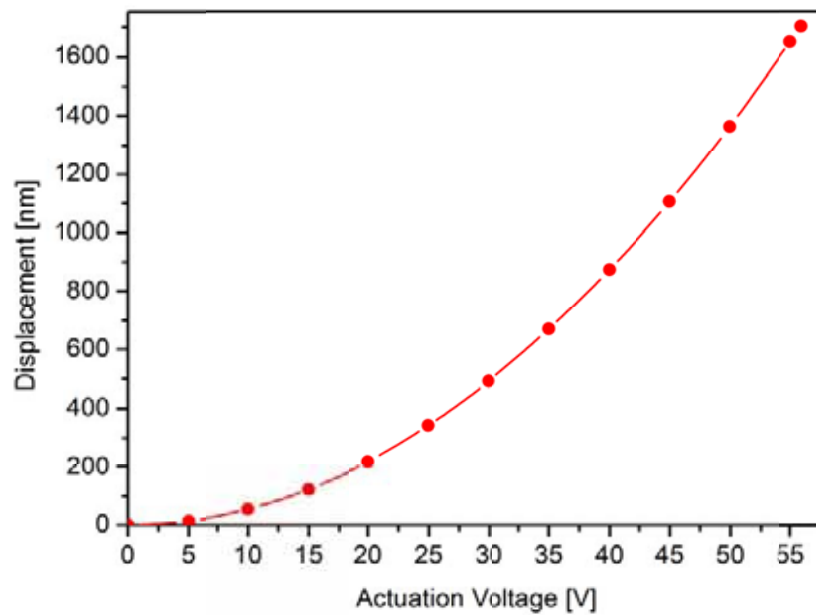

Figure 13: *Calculated displacements for various voltages for the designed actuator.*

2.1.4. Fabrication

Displacement sensors are fabricated in order to confirm results of the numerical study experimentally. First, sensor geometries are patterned using electron beam lithography (FEI Nova NanoSEM 600 with integrated Raith ElphyPlus, FEI&Raith Co.). A positive electron beam resist (PMMA 950K, Microchem Co.) is spin coated. The largest dimension of device pattern takes place at the anchor of the actuator, 500 µm, whereas, the critical dimension (CD) occurs at the spring width, 200 nm. In order to minimize writing time in electron beam lithography without compromising pattern quality at both extremes, consecutive two patterns are written using mix-match process. The recipe of large and small pattern features utilized in the electron beam lithography processes are given in Table 2.

Table 2. Electron beam lithography parameters.

Electron Beam Resist Patterning Recipe			
Positive resist (PMMA) Deposition of Small Features	Prebake	180 ºC	2 min
	Spin coat	750 rpm	10 sec
		1500 rpm	1 min
	Postbake	180 ºC	2 min
	Resist Thickness	100 nm	
Patterning Small Features	Acceleration Voltage	30 kV	
	Beam Current	69 pA	
	Step Size along x, y	10 nm	
	Exposure Density	240 µC/cm^2	
	Write Field Size	50µm × 50µm	
Development	Developing by 1:3 MIBK:IPA	25 ºC	50 sec
	Rinsing by IPA	25 ºC	20 sec
	Postbake	100 ºC	1 min
Positive resist (PMMA) Deposition of Large Features	Prebake	180 ºC	
	Spin Coat	800 rpm	10 sec
		1700 rpm	1 min
	Postbake	180 ºC	2 min
	Resist Thickness	80 nm	
Patterning Large Features	Acceleration Voltage	10 kV	
	Beam Current	2.58 nA	
	Step Size along x, y	500 nm	
	Exposure Density	100 µC/cm^2	
	Write Field Size	1000µm × 1000µm	
Development	Developing by 1:3 MIBK:IPA	25 ºC	50 sec
	Rinsing by IPA	25 ºC	20 sec
	Postbake	100 ºC	1 min

The displacement sensor is fabricated on an SOI wafer with 260nm-thick device silicon and 2µm-thick buried-oxide layer. Process plan is illustrated in Fig. 14.
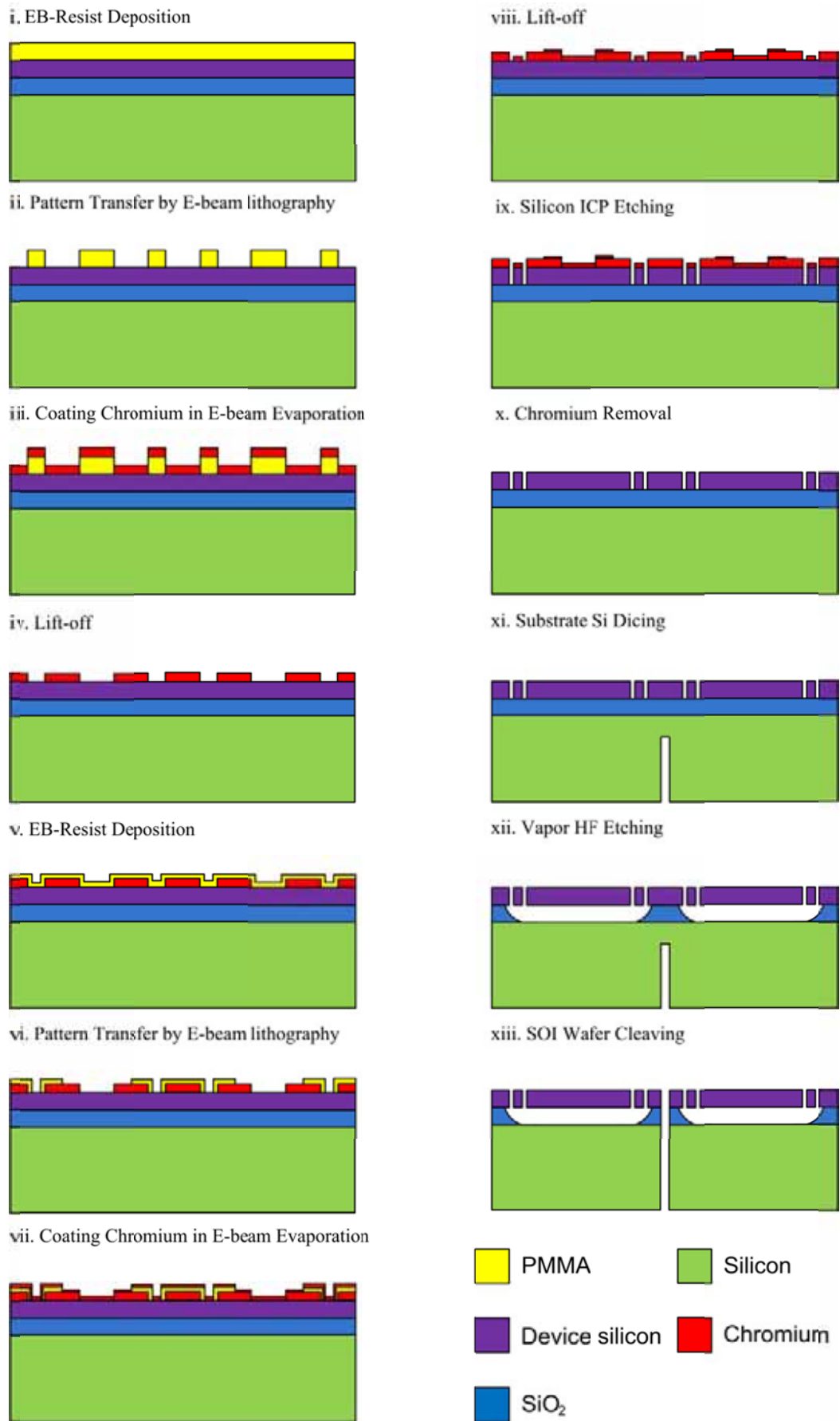
i. EB-Resist Deposition

ii. Pattern Transfer by E-beam lithography

iii. Coating Chromium in E-beam Evaporation

iv. Lift-off

v. EB-Resist Deposition

vi. Pattern Transfer by E-beam lithography

vii. Coating Chromium in E-beam Evaporation

viii. Lift-off

ix. Silicon ICP Etching

x. Chromium Removal

xi. Substrate Si Dicing

xii. Vapor HF Etching

xiii. SOI Wafer Cleaving

PMMA   Silicon

Device silicon   Chromium

SiO₂

Figure 14: *Process plan of the displacement sensors.*

"NANO-DISP"

First, electron beam lithography of small features on PMMA is completed. Next, metallization with chromium by electron beam evaporation (PVD Vapor 4S E-Beam, Vaksis Co.) for lift-off is employed. Then, large features are patterned as the second mask layer on PMMA. Parameters utilized in both evaporation steps are as presented in Table 3.

Table 3. Electron beam evaporation parameters.

Chromium Deposition for Lift-off		
Small Features		
Preparation	Chamber Vacuum	4×10^{-6} Torr
	Chromium Density	7.19 g.cm^{-3}
	K Factor	100
	Ionization Energy	2987 kJ.mol^{-1}
	Temperature	20 ºC
Deposition	Voltage	35 kV
	Current Beam	25 mA
	Rate	0.03 nm/s
	Thickness	50 nm
Drying	Dry N$_2$ Gas	1 min
Large Features		
Preparation	Chamber Vacuum	5×10^{-6} Torr
	Chromium Density	7.19 g.cm^{-3}
	K Factor	100
	Ionization Energy	2987 kJ.mol^{-1}
	Temperature	20 ºC
Deposition	Voltage	50 kV
	Current Beam	25 mA
	Rate	0.06 nm/s
	Thickness	30 nm
Drying	Dry N$_2$ Gas	1 min

Table 4. Inductively-Coupled-Plasma Deep-Reactive-Ion-Etching (ICP-DRIE) parameters.

Silicon DRIE Recipes		
Recipe	I	II
Number of Cycles	25	
Passivation Time	6 sec	
Etch Time	5 sec	
Chamber Vacuum	8×10^{-3} Torr	10×10^{-3} Torr
SF$_6$/O$_2$ Flow Rates	20/50 sccm	
RF Platen Power @ Etch/Passivation	600/20 W	300/10 W
RF Generator Power @ Etch/Passivation		

Then, after remaining PMMA resist is removed, device silicon layer is dry etched by inductively coupled plasma (LPX SR-Cl, STS Co.) using SF_6 and O_2 gases. Chromium is utilized as a hard mask due to its high selectivity with respect to silicon. Table 4 lists the parameters utilized in the inductively-coupled-plasma deep-reactive-ion-etching (ICP-DRIE) process. 260nm-thick device silicon is etched with 74.18 nm/min etch rate.

Figure 15 depicts scanning electron microscopy (SEM) images taken for devices etched using Recipe 1 and 2. Ionization energy affects etch rate and smoothness of sidewalls. In Recipe 1, silicon sidewalls are over etched causing large scallops as seen in Figs. 15a and 15b. Figure 15c shows that due to high etch rate, the straight waveguide is damaged and lifted off the BOX layer. In Recipe 2, where RF platen and generator powers at etch and passivation steps are optimized, however, silicon sidewalls are smooth as seen in Figs. 15d and 15e with scallops of around 20 nm. Properly fabricated straight waveguide as a result of use of Recipe 2 is as shown in Fig 15f.
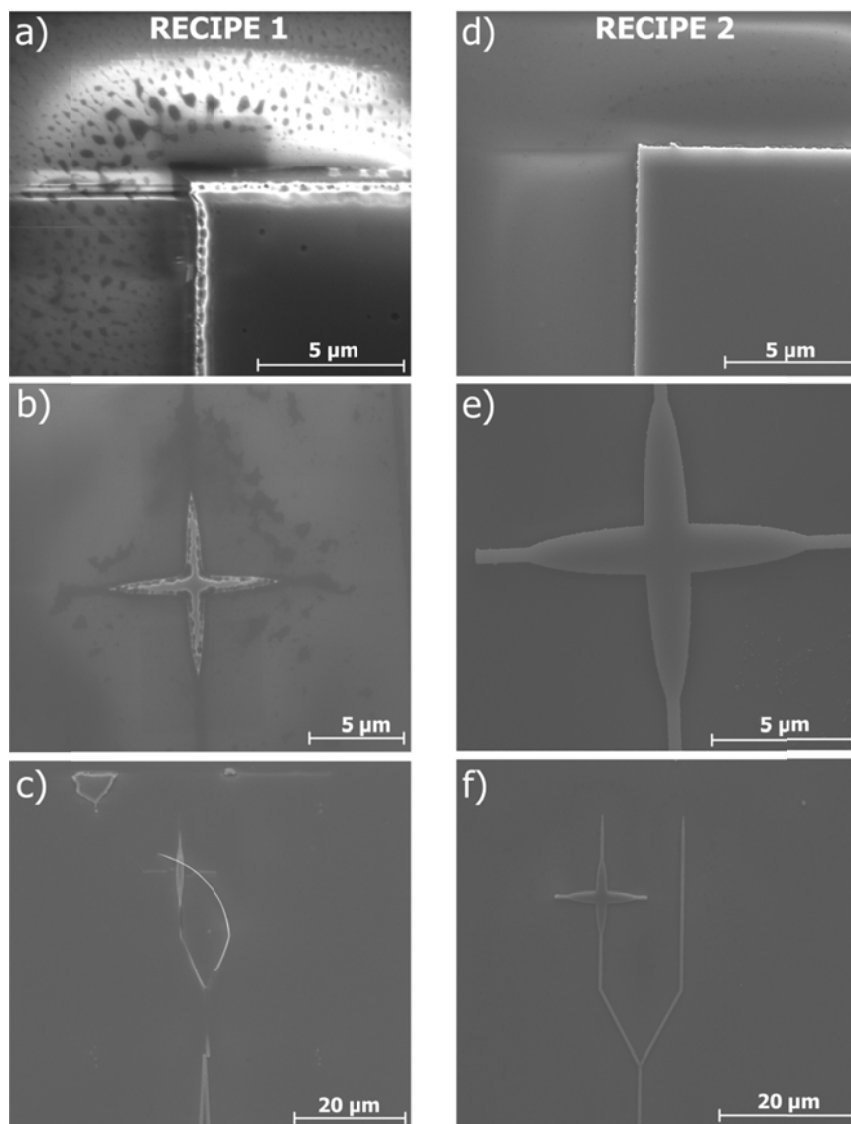

Figure 15: *Comparison of a failed and succeeded ICP-DRIE recipes. a) Silicon sidewalls with large scallops, b) overetched elliptical intersection geometry, c) lifted off straight waveguide, d) smooth silicon sidewalls, e) smooth elliptical geometry, and f) smooth straight waveguide.*

Studied sensors are fabricated in order to understand characteristics and confirm results of the numerical study experimentally. Figure 16, for example, illustrates SEM micrographs of a typical sensor fabricated prior to device release by Vapor HF Etching. The sensor geometries are successfully etched into silicon down to SiO_2 layer. In addition, tip angles are manufactured precisely. As it can be seen from Figs. 16d and 16e, critical dimension at sensor springs and actuator fingers with 200 nm are properly fabricated. Footprint of the devices, as seen in Fig. 16a, is 1mm × 2mm. What in reality will be integrated into the applications is indeed only the region 50μm × 80μm in size.
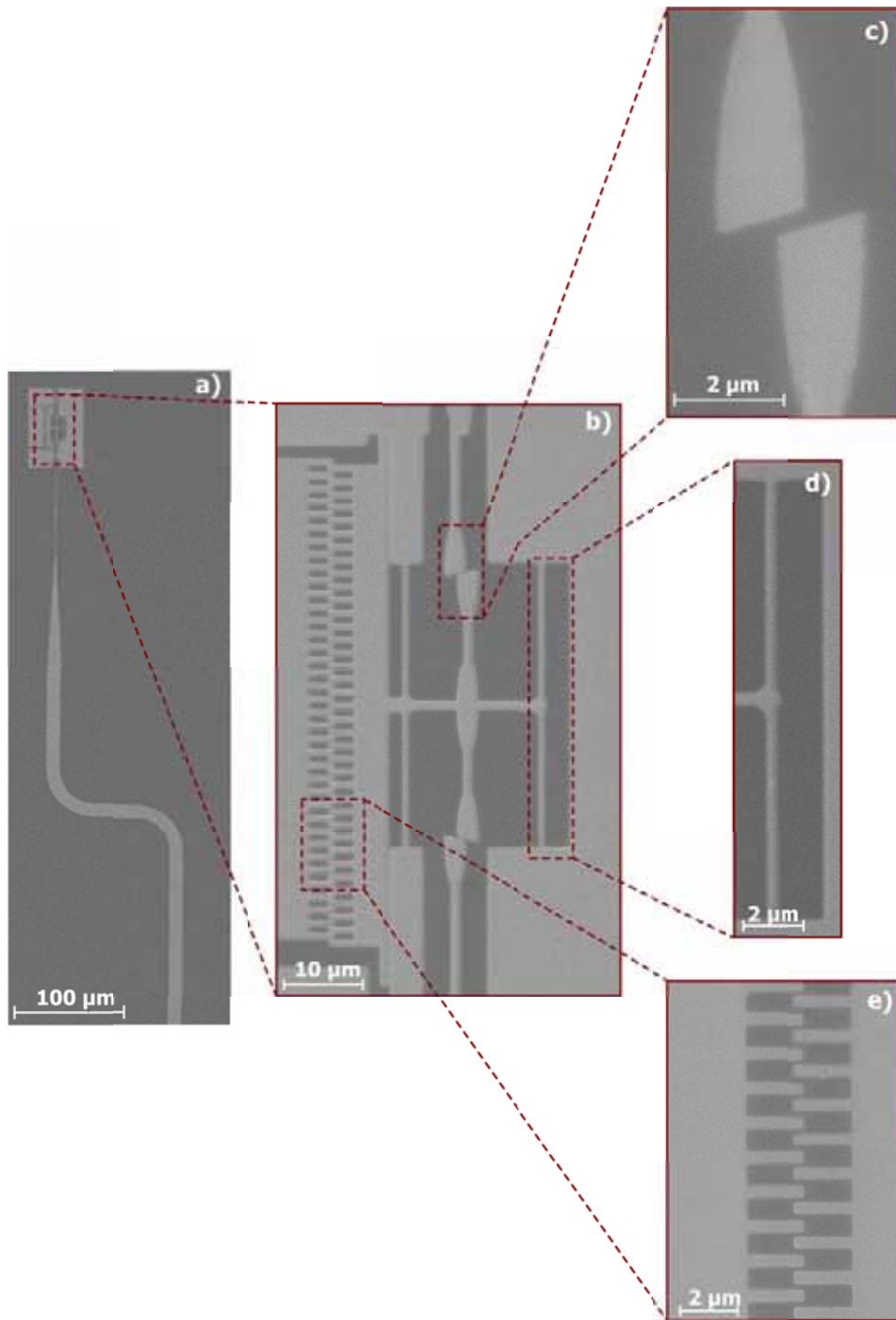

Figure 16: *SEM micrographs of the fabricated sensor. a) Overall sensor prototype, b) sensor embedded into the actuator as the source of motion, c) elliptical tip, d) spring, e) actuator fingers.*

Both matching small and large features laterally in position, and, as discussed meticulously in "2.1.5. Vapor HF Setup Design and Fabrication" section of this report, manufacture of Vapor HF Etching Setup towards device release are estimated to be completed simultaneously within two months. Afterwards, fabricated sensors will be characterized in the mechanical and optical setups, which are being procured and installed from a subsequent fund, approximately 160K Euro for a term of 36 months total, awarded by the Scientific and Technological Research Council of Turkey (TUBITAK). As soon as the device release of the sensors is completed fully, measurements will be conducted in the characterization setups as given in detail in "2.2. Installation of Device Characterization Setups" section of this report.

2.1.5. Vapor HF Setup Design and Fabrication

Vapor HF Etching Setup is used for device release by etching SiO_2 as the last step of microfabrication of displacement sensors [4]. Etch rate is dependent on wafer temperature. Thus, wafer temperature is being controlled during the etching process. 3D solid model of the assembled setup and its realized temperature control unit are as illustrated in Figs. 17a and 17b, respectively. Liquid hydrofluoric (HF) acid in 51% DI water concentration is put into a container, and vaporized by heating. Vapor HF is forced to travel into the setup channels with a certain speed and temperature using nitrogen gas so that it will interact chemically and etch BOX layer windows opened on SOI wafer during microfabrication [5]. All heating tasks are accomplished via flat rubber heaters, which are both small and lightweight.
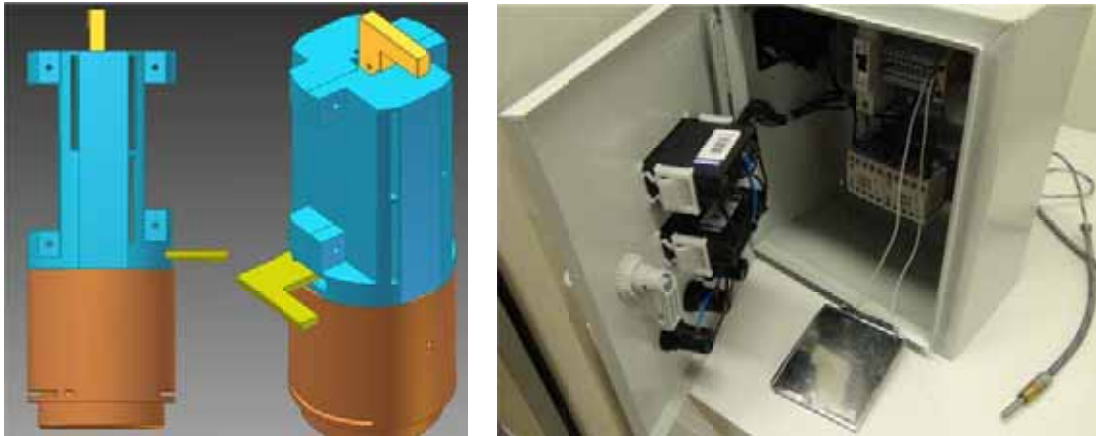

Figure 17: *a) 3D solid model of the assembled Vapor HF Etching Setup design, b) Temperature control unit.*

Polytetrafluoroethylene (PTFE, commercially known as Teflon) is used as the main material because of its high resistance against hydrofluoric acid. Bottom of the Vapor HF Setup is a container for liquid hydrofluoric acid. The container has an input and an output, which direct vapor HF from its source to the wafer being etched with the help of nitrogen gas at a flow rate of 10 ml/min. A flow meter with a manual valve is deployed to observe and control flow rate of nitrogen gas. The main body of etching is designed as the assembly of four components, front body, rear body, container, gate, and wafer holder as illustrated in Figs. 18a through 18e in order. While front and rear body form the etch channel into which the wafer will be placed, gate and wafer holder are used to start and stop HF etching, and to mount wafer into etch channel.
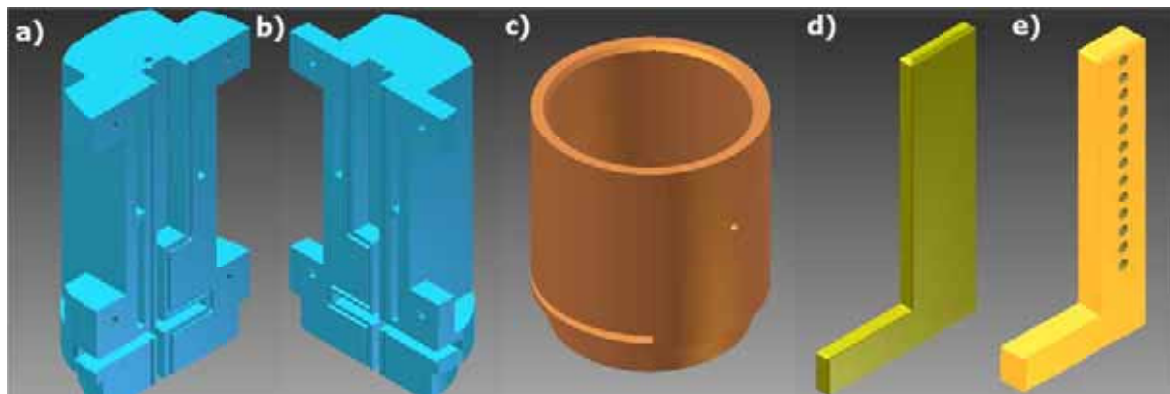

Figure 18: *3D solid models Vapor HF Etching Setup design components. a) Front body, b) rear body, c) container, d) gate, e) wafer holder.*

Figure 19 depicts manufactured components of Vapor HF Setup. Assembly of the setup is as seen in Fig. 20. Etch rate versus wafer temperature curve of the setup will be generated as a calibration curve to guide different possible future users. It is expected to take two months until the characteristics of the setup will be available as of now in mid-November, 2011.
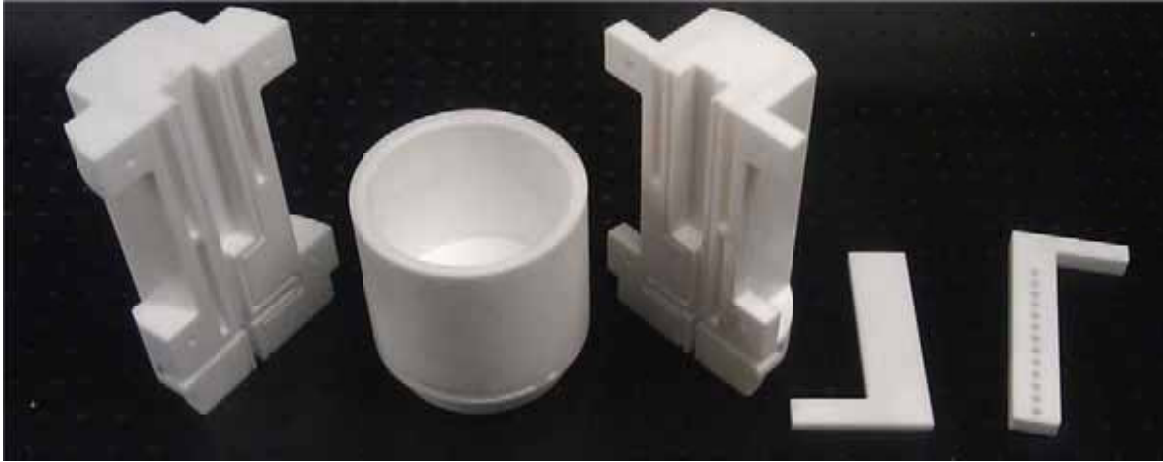

Figure 19: *Fabricated setup components.*

Figure 20: *Assembled setup.*

2.2. Installation of Device Characterization Setups

In order to test the sensors, two characterization setups are needed: Mechanical Characterization Setup and Optical Characterization Setup. Both the mechanical and optical characterization setups are fixed on a passive pneumatic damping optical table 2.4m × 1.2m × 0.2m in size. The mechanical setup is mainly for the purpose of characterizing the mechanical actuation of the devices and observing the dynamic properties of the devices using an optical microscope. The main task of the optical characterization setup, on the other hand, is to observe the optical characteristics of sensors as nanophotonic devices using a Near-Infrared (NIR) camera when the device is excited by a lensed optical fiber. Both of the characterization setups mentioned are as expressed briefly below.

2.2.1. Mechanical Characterization Setup

The main body of the mechanical characterization setup is consisted of a optical microscope with its halogen lamp illuminator and microstages, as seen in Figs. 21a and 21b. The microscope comes with 5x, 10x, 20x and 50x visible-wavelength objectives mounted on the optical microscope using a quadruple turret, and a reflected light measuring stage of 150mm × 150mm in area with 50mm × 50mm X-Y movements. The whole setup is designed to observe the mechanical movement of the actuator under the operation when the voltage is applied. It uses three needles with the tip radius less than 100 μm to physically apply voltage. The needles are mounted on microstages via custom needle holders fabricated on epoxy glass sheets. It uses four microstages each with a footprint of 40mm × 40mm. Each microstage can move 50 mm in all XYZ directions with the resolution of 10 μm, and have a capacity to handle 3 kgf load vertically. All microstages are fixed on a plate under the optical microscope.
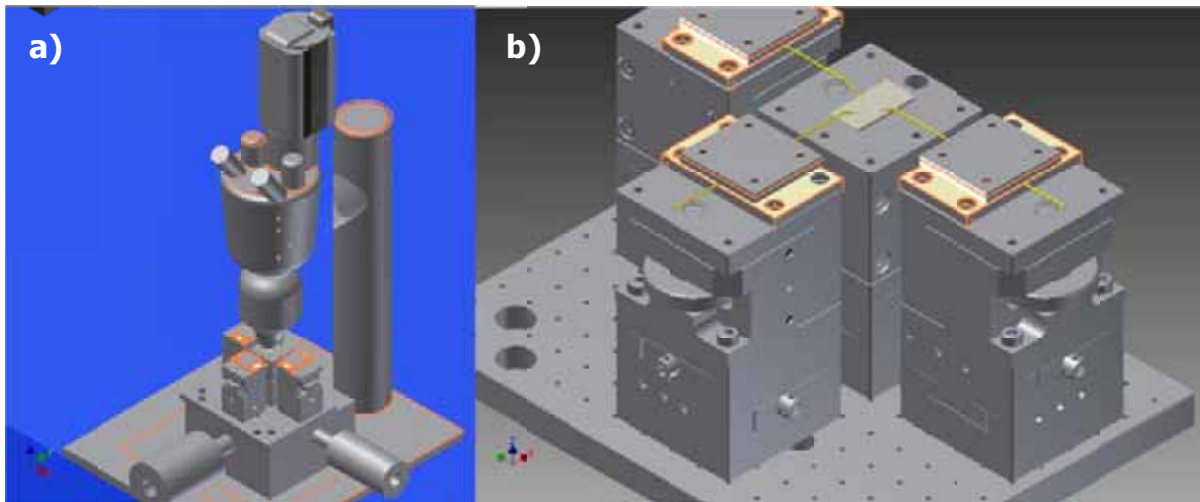

Figure 21: *Schematic 3D views. a) The mechanical characterization setup, b) how the mechanical actuation is achieved.*

The actuation power is provided by a signal generator, whose output is amplified using a 5 MHz DC high voltage piezoamplifier. A high-definition visible camera is mounted on the microscope using C-mount connection so as to observe and record motion generated by the actuator in the sensor. The mechanical characterization setup is shown in Fig. 22.
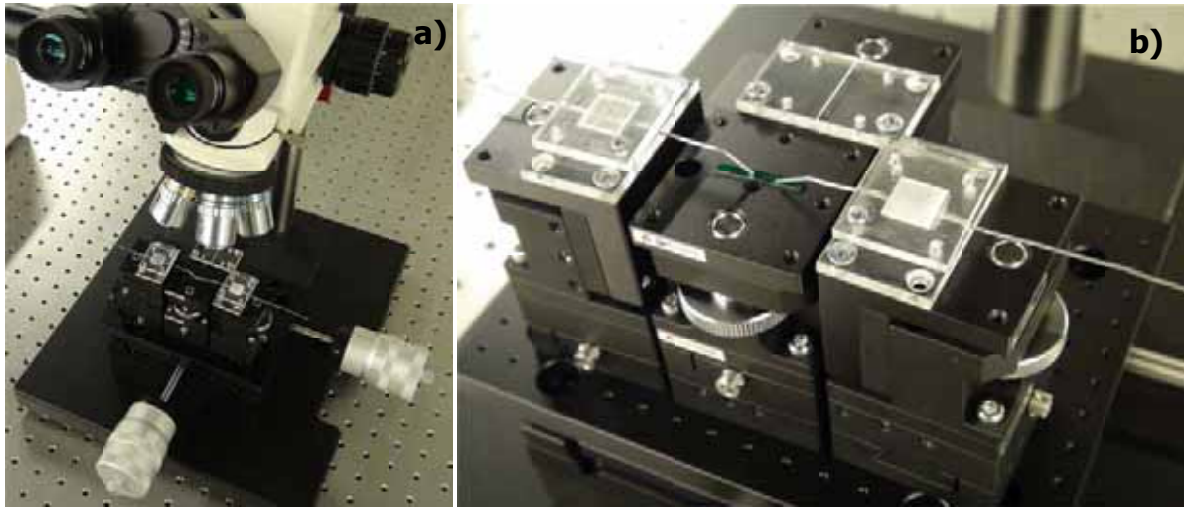
Figure 22: *The mechanical characterization setup. a) Optical microscope under which the mechanical characterization setup is implemented, b) how the mechanical actuation is achieved.*

2.2.2. Optical Characterization Setup

Optical characterization setup is consisted of two main units: 1) NIR Imaging System, and 2) Mechanical Adjustment System. Main goal of the setup is to observe and characterize the optical properties of the sensors under the test. Optical characterization setup, as shown in Fig. 23, is designed in 3D Solid Modeling Software (Mechanical Desktop Inventor®, Autodesk Co.).
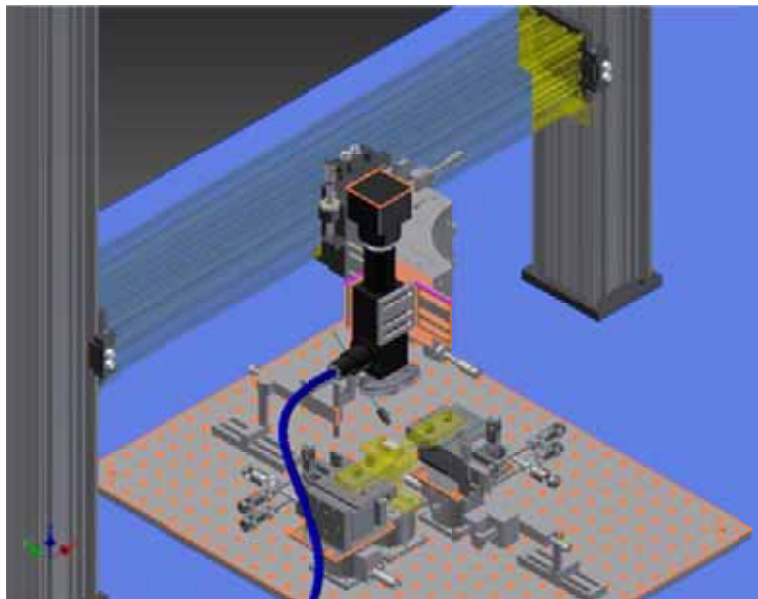

Figure 23: *3D solid model of the optical characterization setup.*

In order to protect both personnel and equipment from possible damage during the experiments, certain safety measures in the laboratory such as laser goggles for both visible and infrared wavelength spectrum, IR and UV sensor cards are taken. In addition, for a flexible and robust lab environment in order to conduct complex experiments such components as optical posts and clamps in different sizes, extension platforms, thread adapters, breadboard lifting handles, and base plates are procured.

2.2.2.1. NIR Imaging System

The system is mainly set up in order to manipulate the NIR camera and observe optical output of sensors during characterization. An Optical Spectrum Analyzer (OSA) works as a tunable laser to provide the polarized light field for the device testing and characterization. The light field is coupled to the input port of the waveguide through lensed optical fiber with a conically tapered tip at one end resulting 6μm ± 0.5μm spot size. The other end is FC/PC with an overall length of 2 m. Remaining 30-50mm-long bare fiber is protected with a 900 μm sleeve.

As shown in Fig. 23, a solid state InGaAs sub-wavelength Infrared (SWIR) Camera is employed to observe the optical response of the sensors in NIR wavelength region. The camera is connected to a PC in order to observe the video to implement image processing to calculate the light intensity on the sensor as the indirect measurement result. The camera is placed on a Video Microscope Unit (VMU) with a C-mount connection. A high resolution video microscope has specifically been designed for viewing small electronic and electromechanical components, and waveguides requiring high magnification visual inspection. The VMU uses coaxial in-line illumination fed by a tunable 150W halogen lamp light source with variable intensity control. On the other side of the video microscope, a quadruple turret for the objectives is mounted in order to achieve the desired magnification in the optical system. 10x, 20x, 50x and 100x M Plan Apo NIR objectives are assembled to the NIR optical system via the turret.

The video microscope is fixed and mounted with L-shaped clamps on an XYZ translation stage that can move maximum 50 mm in all XYZ directions with a load capacity of 18 kg vertically. The translation stage has the capability of coarse and fine position adjustment with a high resolution. The translation stage is mounted on another stage to offer longer travel ranges to the system in Z axis. The Z translation stage is mounted on a carriage that lets the system to move along the construction rail. As shown in Fig. 24a, a profile support system to enable adjustment of the NIR camera right up on the tested sensor device using optical construction rails and carriages. A custom holder, as shown in Fig. 24b, is designed and fabricated to mount VMU to the Z axis translation stages.
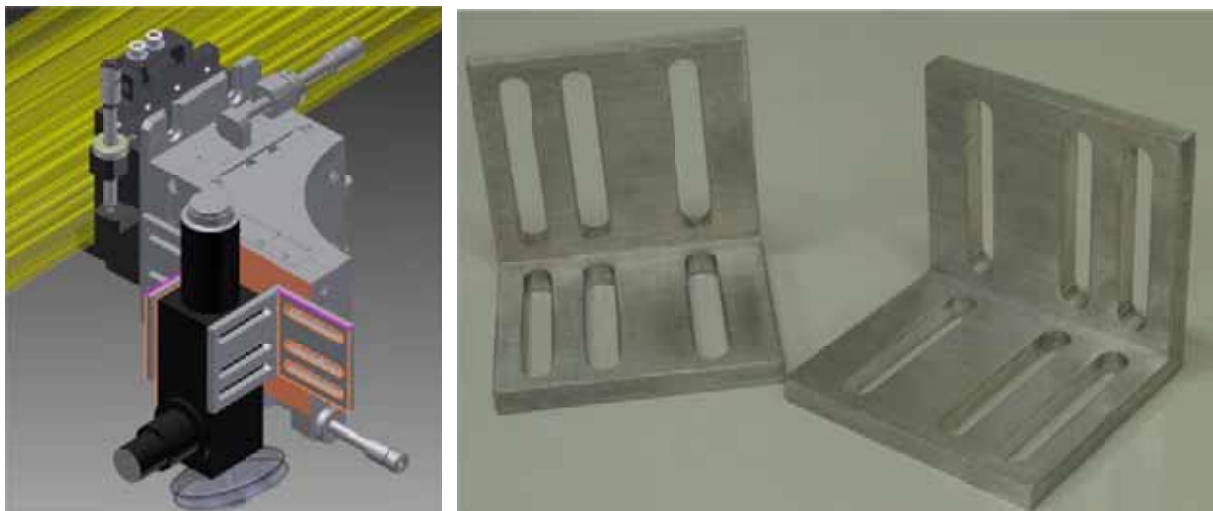

Figure 24: *a) NIR imaging system carried by profile support system, b) custom VMU holder.*

2.2.2.2. Mechanical Positioning System

The mechanical positioning system is consisted of several stages and manipulators to provide excitation for both optical and electrical systems as seen in Fig. 25. The sensors are going to be fixed on a standard waveguide mount placed magnetically on top of a standard platform with a 62.5 mm standard deck height. In order to make it easier and more flexible to couple the light field to the input port of the waveguides on the device, two tapered V-groove fiber holders with magnetic clamps on each fiber holder are used to fix the optical fiber. Four-axis low-profile micro-block device platform stages with four independent degrees of freedom (DOF) provide 13 mm of horizontal translation, 6 mm of vertical translation, 10º of pitch and 10º of yaw rotations. These stages with a fine travel resolution of 50 nm in horizontal and vertical axes and of one arcsec in yaw and pitch axes are designed for precise orientation of nanophotonics components and planar devices alike. With the help of three Z axis aluminum ball slide stages, the two micro-block stages and the standard platform are enabled to move 10 mm vertically with an accuracy of 10 μm.
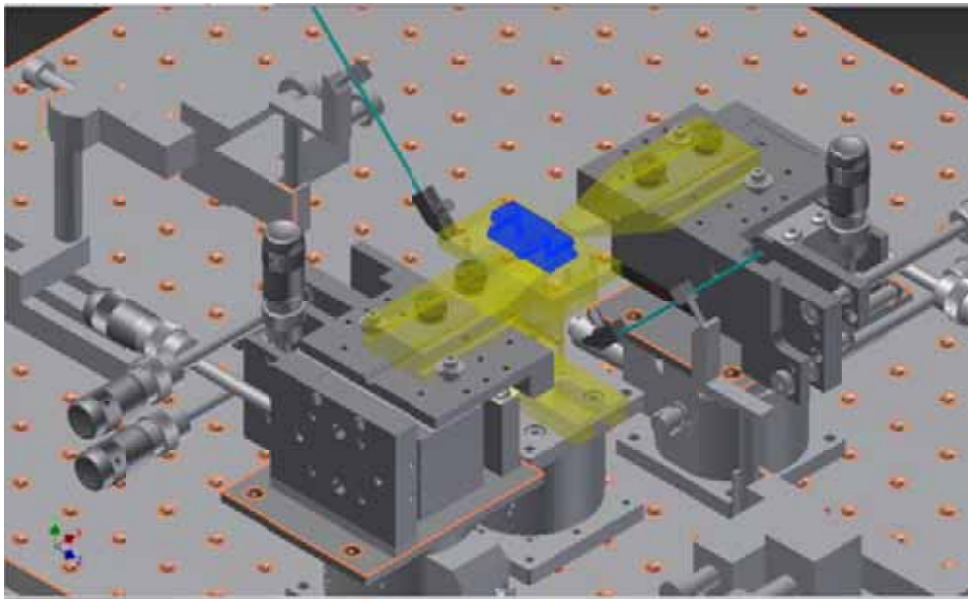

Figure 25*: Mechanical positioning system.*

Two micromanipulators are used to apply voltage through needle probes to the nanophotonics sensors. For portability and ease of use, all of the stages and manipulators are fixed on an aluminum breadboard 450mm × 600mm × 12.7mm in size.

3. PHASE 2

In PHASE 1, displacement sensors with large-range low-sensitivity characteristics are studied and are about to be experimentally verified soon. On the other hand, in this phase, design, fabrication and characterization of short-range high-sensitivity in-plane displacement sensors is being realized in order to clarify the practical limits of highest-sensitivity and shortest-range achievable. Towards this goal, two main types of sensor approaches are currently under investigation as presented below.

3.1. Normally-off Short-range High-sensitivity Physical Contact Displacement Sensor TYPE 1

Having found limits of largest-range and lowest-sensitivity in the sensors investigated in PHASE 1 with elliptical tip geometry, tip angle and length are understood to be main drivers setting the character. While sensors based on elliptical tip geometry yielded large-range low-sensitivity features for tip angles above the Brewster's, same tip geometry with tip angles below the Brewster's promise to be good candidates for short-range high-sensitivity ones.

3.1.1. Sensor Principle

First type of short-range high-sensitivity sensors herein is based on the fundamental concept of those utilizing elliptical tips as in PHASE 1, but with tip angles below the Brewster's as emphasized above. Also, results in PHASE 1 have proved that the highest contrast in transmittance occurred at 4.8 μm length of elliptical tip. Hence, for instance, such an elliptical sensor geometry with 40º angle, 4.8 μm length and 1.5 μm width causes transmittance of 97.78% at 0 nm, 37.16% at 100 nm distances provided 1.24 nm per percent of light intensity. Accordingly, Figure 26 illustrates the waveguide tip pair modeled in TYPE 1 to figure out effects of the contact-tip geometry on optical properties. As shown in Fig. 26, the distance measured is in the direction transverse to light propagation, D. An electrostatic comb drive similar to that discussed in PHASE 1 will be employed as the source of motion for changing distance, D, values to imitate real-life applications.
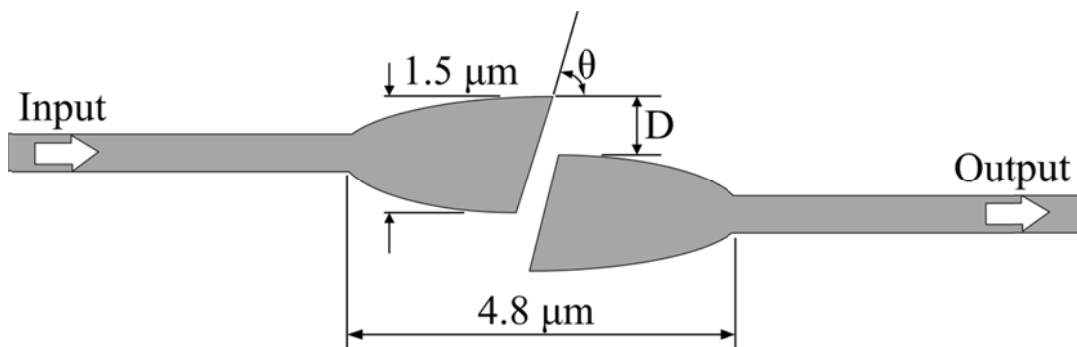

Figure 26: *Schematic view of TYPE 1 tip geometry for short-range high-sensitivity displacement sensing.*

3.1.2. Numerical Study in FDTD

Displacement sensor simulations of this particular type are numerically conducted in 3D FDTD analysis software. For single-mode TE-polarized light at 1.55 μm wavelength, waveguide width and thickness are 500 nm and 260 nm, respectively. Elliptical tip geometry is 1.5μm-wide, 4.8μm-long, and 260nm-thick. Various tip angles of 10º, 20º, 30º, 40º, 50º, 60º, 70º, and 80º are studied for short-range displacement values of 25 nm, 50nm, 75nm, 100nm, 200 nm, 300 nm, and 600 nm. Results are shown in Figs. 27 and 28.

Data depicted in Fig. 27 suggest that the smaller the tip angle, the higher the sensitivity. While at 40º tip angle, for example, the sensitivity is 1.24 nm per percent of light intensity, it is expected to be less than 1.24 nm per percent of light intensity for elliptical tips with angles smaller than 40º. However, such geometries, as it can be seen from the A-A inset in Fig. 27, again because of the very same reason, are highly dependent on gaps left between contact-tips owing to their sidewall surface roughnesses.
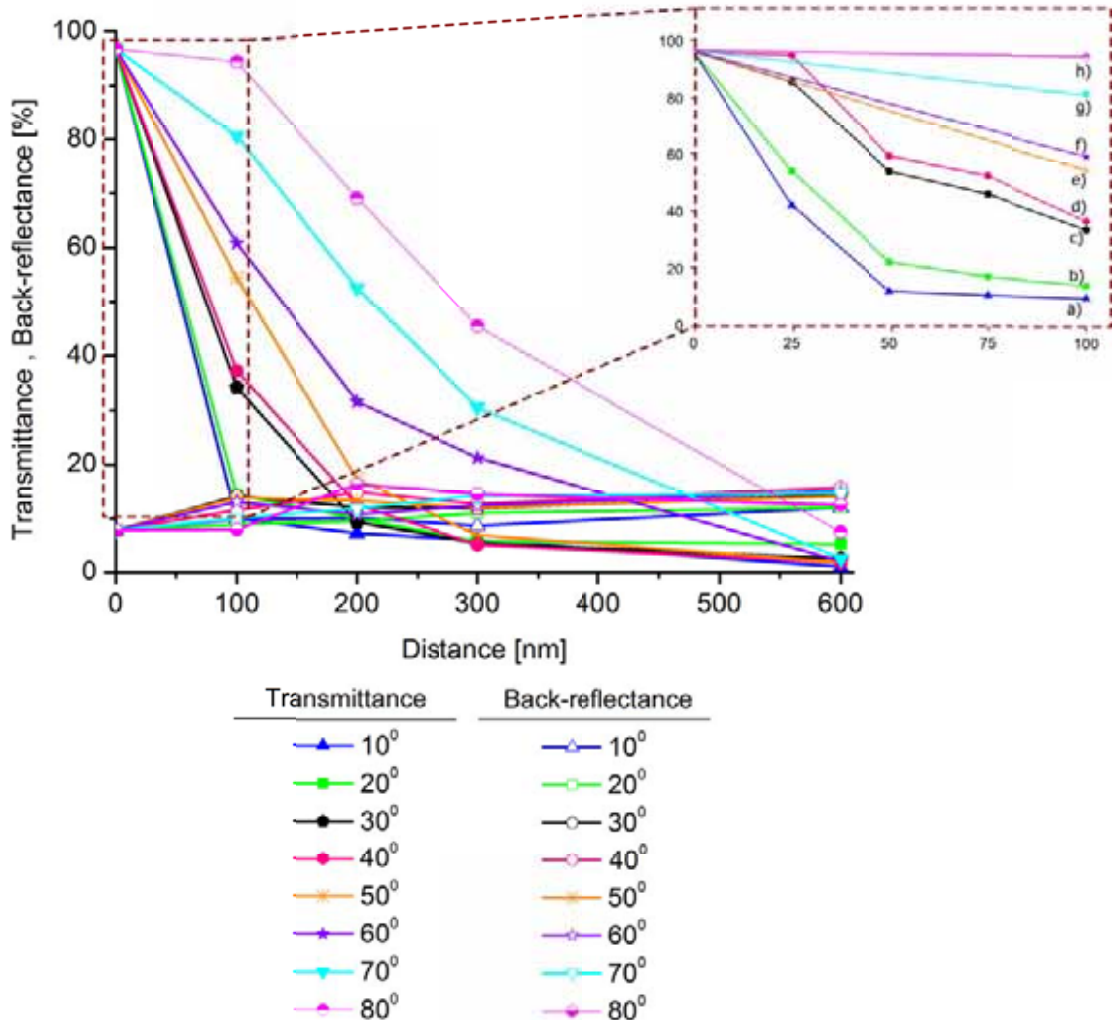

Figure 27: *Calculated transmittance and back-reflectance as a function of distance, D, at the tip angles, θ, of 6.3º, 10º, 20º, 30º, 40º, 50º, 60º, 70º, and 80º for 4.8µm-long and 1.5µm-wide elliptical tip geometry.*

Figure 28 illustrates special points in Fig. 27 at 100 nm for various tip angles to understand behavior of the lightwave as it experiences tip geometry of TYPE 1. The reason why 100 nm distances are particularly looked in detail is because fabrication errors are estimated to be within this distance range. High transmittance above 100 nm is desirable in achieving high-contrast, thereby, high-sensitivity displacement sensors. As seen in Figs. 28a and 28b, at tips with 10º and 20º angles, about 15% of lightwave almost does not propagate to the sensor output. Nevertheless, an acceptably high level, about 40%, of lightwave reaches to the sensor output tip angles from, say, around 30º up to 40º, as presented in Figs. 28c and 28d. As of tip geometries with approximately 50º tip angle and above up to around 60º, a strong portion, about 60%, of lightwave is able to propagate to the output, as depicted in Figs. 28e and 28f, suggesting the last suitable candidate below the Brewster's angle towards realization of short-range high-sensitivity sensor. Tips with angles above 60º even when they are below the Brewster's such as 70º and those above the Brewster's are understood to be inappropriate for

short-range high-sensitivity sensors since most of the light above 80% is able to reach to the output causing very low contrast in transmittance. However, all those above 60º tip angles can be used towards large-range low-sensitivity sensors as noted already in PHASE 1, approving the previous findings.
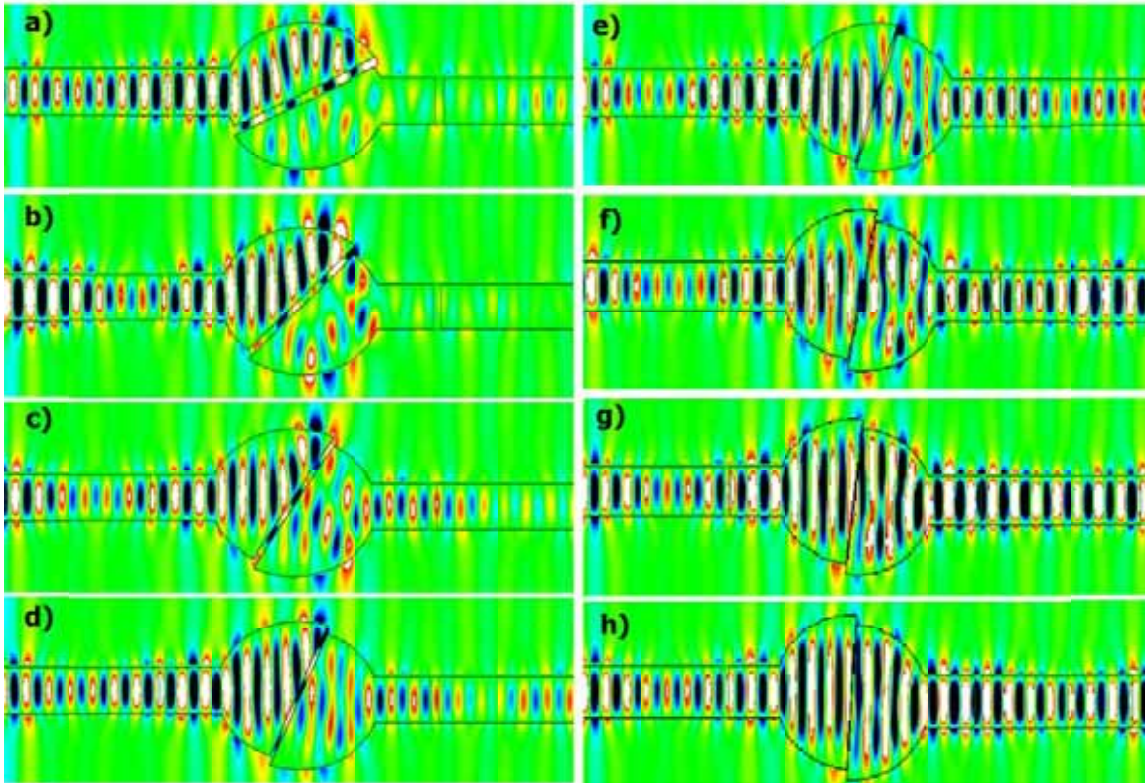

Figure 28: *Electric field (E_x) at 100 nm distance as a function of tip angles at, a) 10º, b) 20º, c) 30º, d) 40º, e) 50º, f) 60º, g) 70º, h) 80º.*

Numerical analysis results showed that at elliptical tips with a length of 4.8 µm, for tip angles of below 10º, 20º, 30º to 40º, and 50º measurement sensitivities of 1.10 nm, 1.24 nm, 3.05 nm, 4.6 nm, and 5.74 nm per percent of light intensity at measurement ranges of 135 nm, 149 nm, 325 nm, 485 nm, and 674 nm, respectively, are observed. Since the surface sidewall roughnesses are expected to be minimized down to about 20 nm total in the tips by precise fabrication, elliptical geometries with the angles in the range from 30º up to 40º will provide the optimal solution for the highest-sensitivity in short-range displacement sensing and measurement in TYPE 1 sensors.

3.1.3. Fabrication

TYPE 1 sensor is fabricated in order to understand characteristics and confirm results of the numerical study experimentally. For instance, Figure 29b illustrates the properly patterned sensor with the decided optimal tip angle of 40º as concluded in "3.1.2. Numerical Study in FDTD." Figure 29 illustrates SEM images of the fabricated sensor prior to device release by Vapor HF Etching. The sensor geometries are successfully etched into silicon down to SiO_2 layer. Tip angles are also manufactured precisely. Critical dimension at sensor springs and actuator fingers with 200 nm are properly fabricated as well. Footprint of the device, as seen in Fig. 29a, is 1mm × 2mm. What in reality will be integrated into the applications is indeed only the region 50µm × 80µm in size.
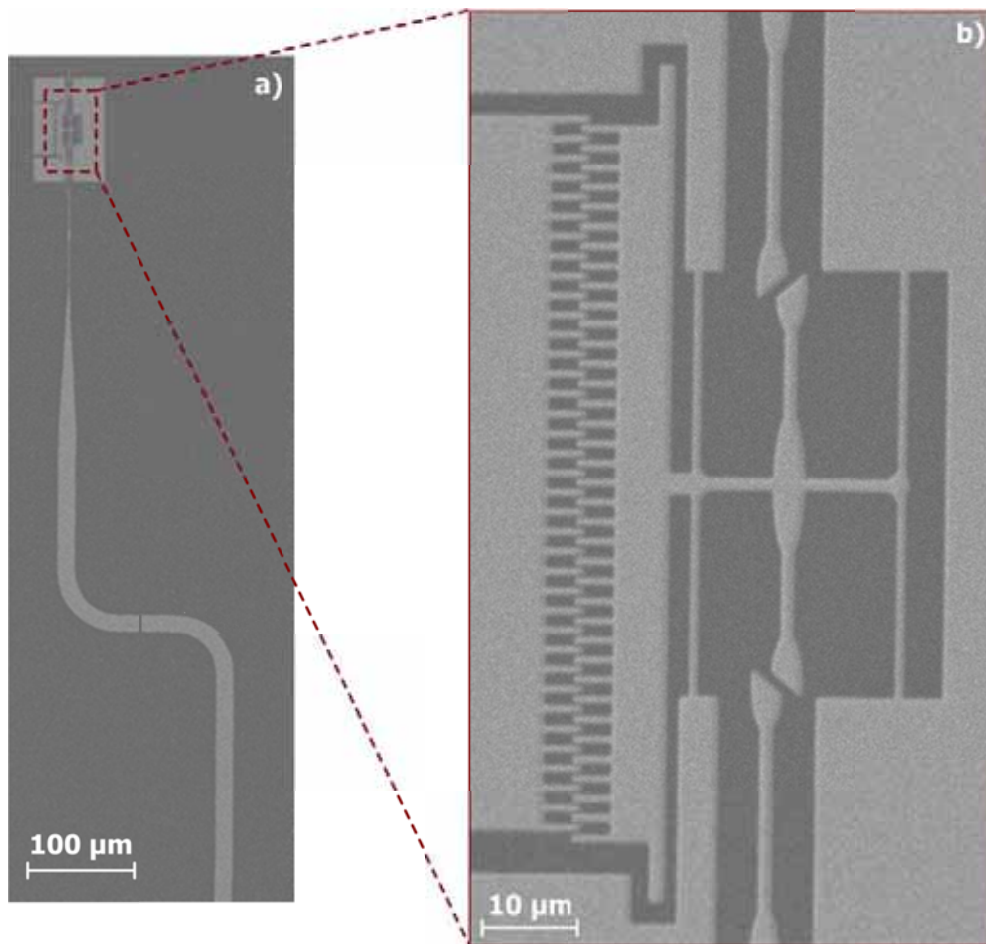
"NANO-DISP"

Figure 29: *SEM micrographs of the fabricated short-range high-sensitivity sensor. a) Overall sensor prototype, b) sensor embedded into the actuator as the source of motion.*

3.2. Normally-off Short-range High-sensitivity Physical Contact Displacement Sensor TYPE 2

The preliminary numerical studies as mentioned already in the project proposal regarding PHASE 2 were promising towards realization of short-range high-sensitivity displacement sensors. Hence, having completed TYPE 1 sensors of PHASE 2, the geometry as shown in Fig. 30 is deployed and investigated as the next design, called as TYPE 2.

3.2.1. Sensor Structure and Principle

As shown in Fig. 30, the sensor structure is composed of two identical waveguides with tapered tips down to a manufacturable abrupt end. The list of parameters for such a sensor design includes tip width, tip-end size, tip angle, and thickness of device silicon. The preliminary numerical study in FDTD analysis, while, for 600 nm tip width, 200 nm tip-end size, 9.5º tip angle, and 260 nm thickness, for example, has shown 93.63% optical transmittance, an extinction down to 40% between 0 nm and 100 nm displacement values, respectively, took place, suggesting high-sensitivity measurement capability in short displacement ranges.
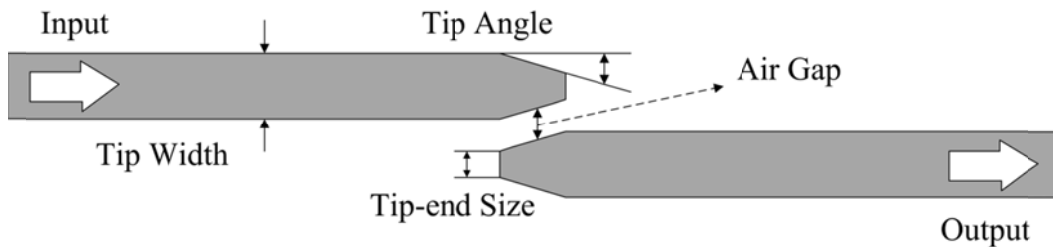

Figure 30: *Schematic view of TYPE 2 tip geometry for short-range high-sensitivity displacement sensor perpendicular to the light propagation distance.*

3.2.2. Numerical Study in FDTD

Various tip widths of 450 nm, 600 nm, 750 nm, and 900 nm, tip-end sizes of 100 nm and 200 nm, tip angles of 8.5º, 9.5º and 10.5º, thicknesses of 170 nm, 200 nm, 260 nm, 380 nm, and 500 nm are simulated at this stage. Outcomes of calculation in FDTD are provided and discussed in the following sections of this report.

3.2.2.1. Effects of Tip-end Size and Tip Angle

Optical performance of TYPE 1 sensor structure is studied at 25 nm, 50nm, 75nm and 100 nm distances, whose results are shown in Figs. 31 through 33. First, for the tip angle of 8.5º, effect of tip-end sizes is investigated. Results are as provided in Fig. 31. When tip-end size is reduced from 200 nm to 100 nm, transmittance gets increased from 85.62% to 96.49% at 25 nm distance, reducing fabrication imperfection dependency. Furthermore, for distances in the range of 25 nm to 100 nm, the contrast in transmittance also increases causing increase in measurement sensitivity as well. Insets in Figure 31 illustrate propagation of lightwave at specific points. Optical performance for the sensor with 100 nm tip-end size at 8.5º tip angle change from 96.49% to 28.72% between 25 nm and 100 nm displacement values, respectively, corresponding to a sensitivity of about 1.10 nm per percent of light intensity.

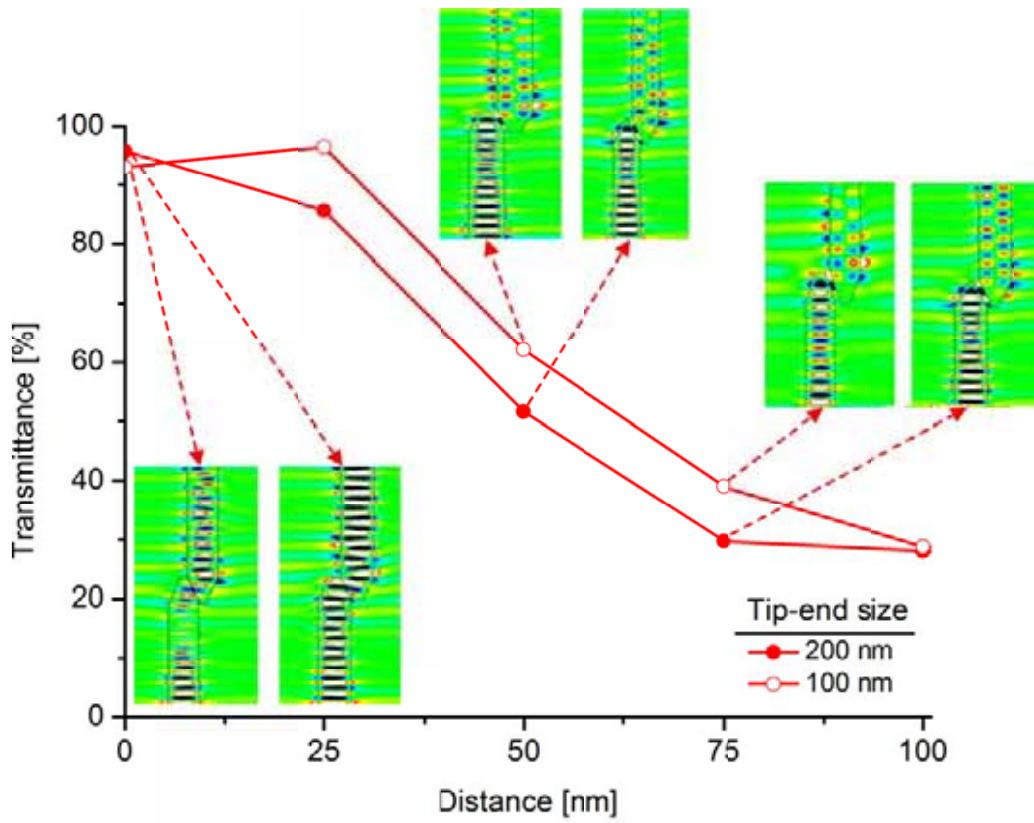**Figure 31:** *Calculated transmittance at the tip angle θ of 8.5° for 100 nm and 200 nm tip-end sizes.*

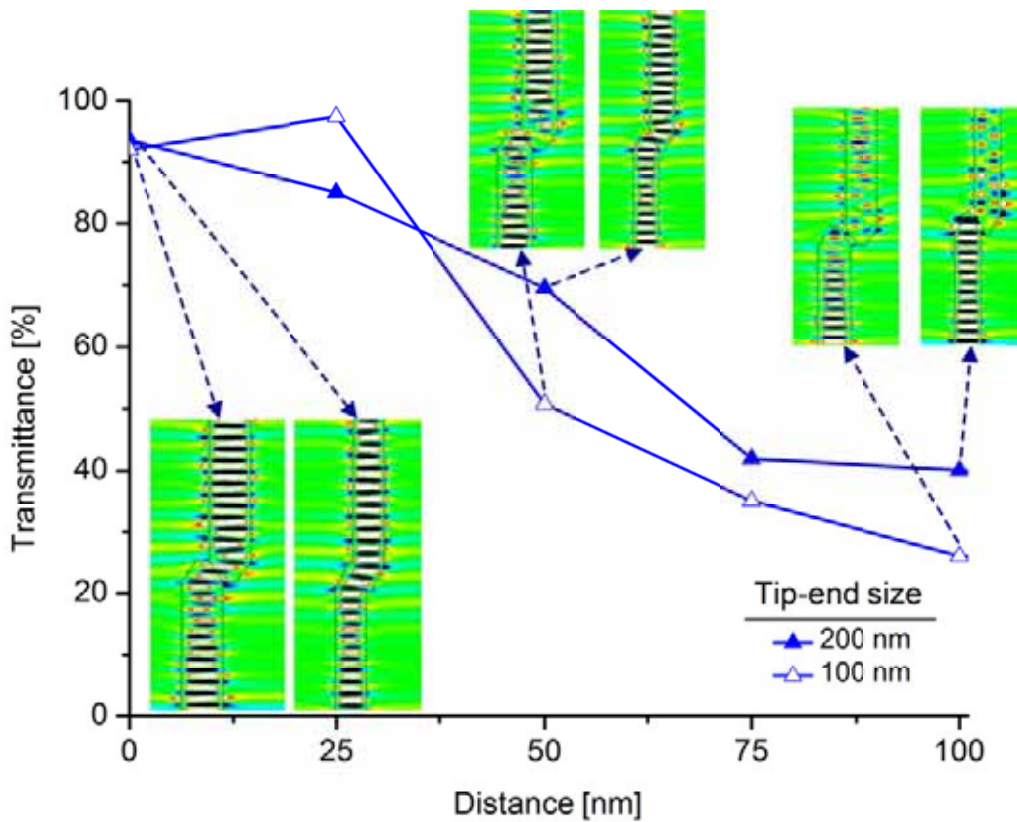**Figure 32:** *Calculated transmittance at the tip angle θ of 9.5° for 100 nm and 200 nm tip-end sizes.*

Next, for the tip angle of 9.5º, effect of tip-end sizes is studied. Results are as depicted in Fig. 32. When tip-end size is reduced from 200 nm to 100 nm, transmittance gets increased from 84.89% to 97.36% at 25 nm distance, reducing fabrication imperfection dependency. Furthermore, for distances in the range of 25 nm to 100 nm, the contrast in transmittance also increases causing increase in measurement sensitivity as well. Insets in Figure 32 illustrate propagation of lightwave at particular points. Optical performance for the sensor with 100 nm tip-end size at 9.5º tip angle change from 97.36% to 25.99% between 25 nm and 100 nm displacement values, respectively, corresponding to a sensitivity of about 1.05 nm per percent of light intensity.

Last, for the tip angle of 10.5º, effect of tip-end sizes is studied. Results are as depicted in Fig. 33. When tip-end size is reduced from 200 nm to 100 nm, transmittance gets increased from 88.25% to 93.14% at 25 nm distance, reducing fabrication imperfection dependency. Furthermore, for distances in the range of 25 nm to 100 nm, the contrast in transmittance also increases causing increase in measurement sensitivity as well. Insets in Figure 33 illustrate propagation of lightwave at particular points. Optical performance for the sensor with 100 nm tip-end size at 10.5º tip angle change from 93.14% to 25.93% between 25 nm and 100 nm displacement values, respectively, corresponding to a sensitivity of about 1.11 nm per percent of light intensity.
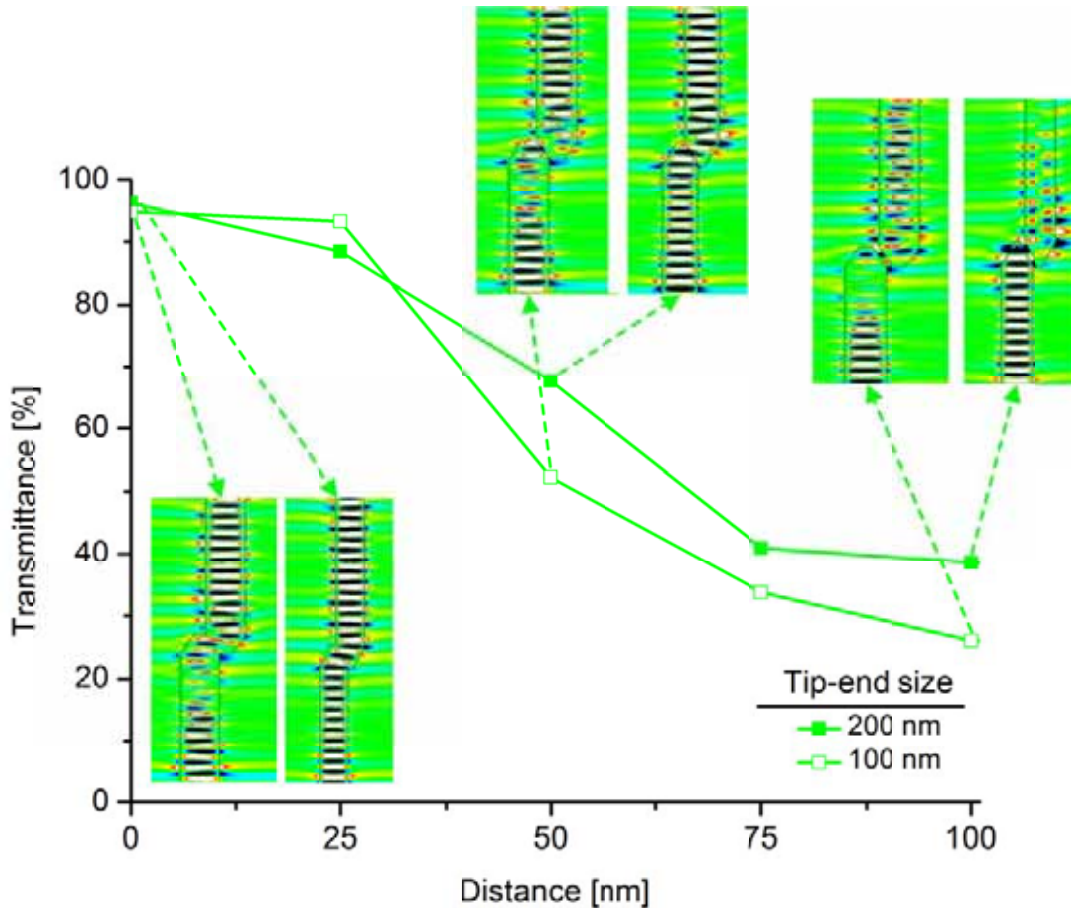

Figure 33: *Calculated transmittance at the tip angle θ of 10.5º for 100 nm and 200 nm tip-end sizes.*

3.2.2.2. Effect of Device Silicon Thickness

After the effects of tip-end size and tip angle on optical characteristics are understood, tip geometries with different thicknesses are investigated. Studies presented in prior sections of this report have employed a thickness of 260 nm in the tip geometry. In this section of the report, however, tip geometries with thicknesses of 170 nm, 200 nm, 380 nm, and 500 nm are deployed to figure out its effect. Herein, tip width and tip-end size are taken 600 nm and 100 nm, respectively. For the tip angles of 8.5º, 9.5º and 10.5º, effect of thickness on contrast in transmittance in the distance range from 0 nm to 100 nm is as given in Fig. 34.
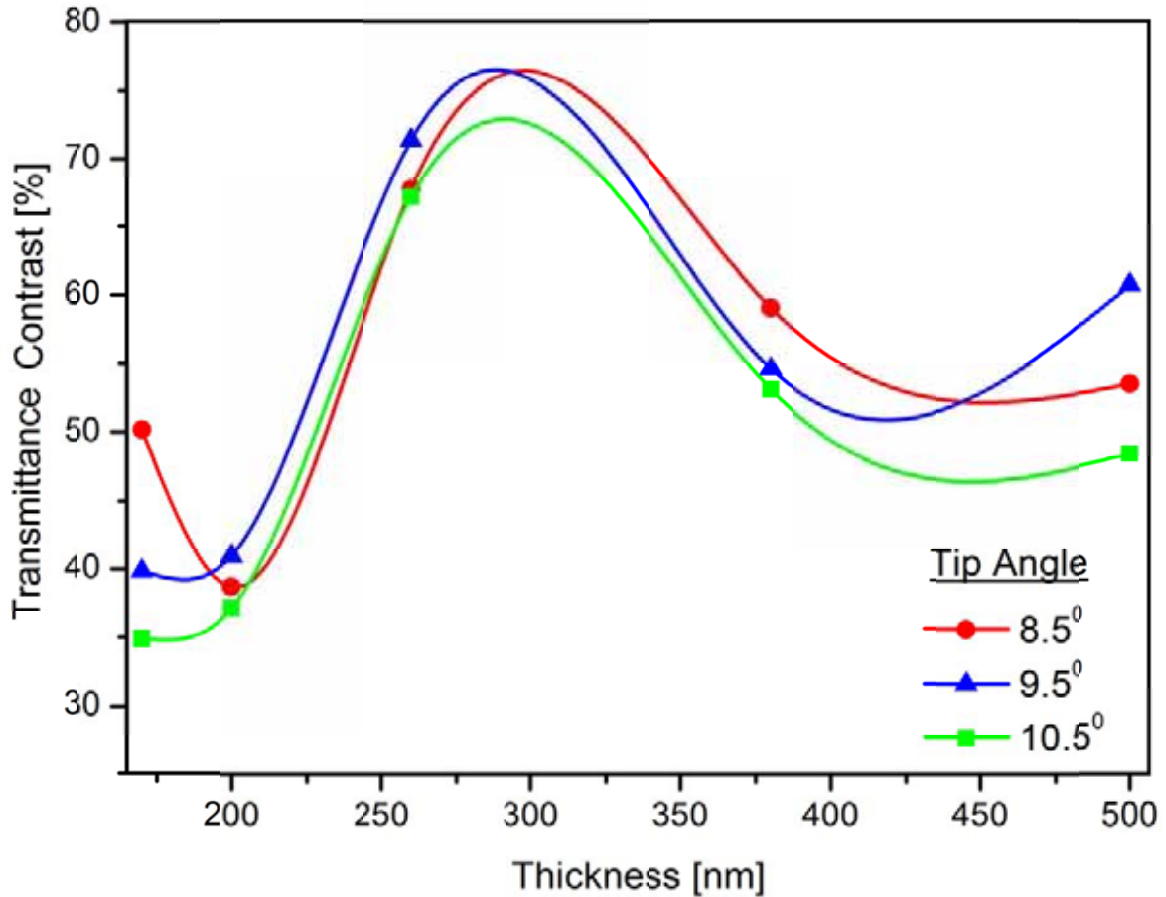

Figure 34: *Calculated contrast at the tip angles, θ, of 8.5º, 9.5º and 10.5º for 170 nm, 200 nm, 260 nm, 380 nm and 500 nm thicknesses of device silicon.*

Data show that peak in transmittance contrast occurs at about 300 nm thickness in the three studied tip angles. The highest sensitivity, hence, at 300 nm thickness is calculated to be 0.97 nm per percent of light intensity when tip angle is in the range of 8.5º and 9.5º. Also, the minimum contrast takes place at 170 nm thickness for 10.5º tip angle. The lowest sensitivity, at this point, is 1.92 nm per percent of light intensity. As aforementioned and it can be seen in Fig. 34, measurement sensitivities of TYPE 2 sensors can be determined in the design stage by proper selection of thickness and tip angle for constant tip width and tip-end size of 600 nm and 100 nm, respectively. Same approach illustrated herein can be applied for various tip widths, tip-end sizes and tip angles to reach optimal thickness for the desired sensitivities and their applications.

3.2.2.3. Effect of Tip Width

After the effects of tip-end size, tip angle, and thickness of device silicon on optical characteristics are understood, tip geometries with tip widths of 450 nm, 750 nm and 900 nm in addition to already studied 600 nm are investigated. Results are as discussed below. Herein, tip-end size and thickness are taken 100 nm and 260 nm, respectively. For the tip angles of 8.5º, 9.5º and 10.5º, effect of tip width on contrast in transmittance in the distance range from 0 nm to 100 nm is as given in Fig. 35.
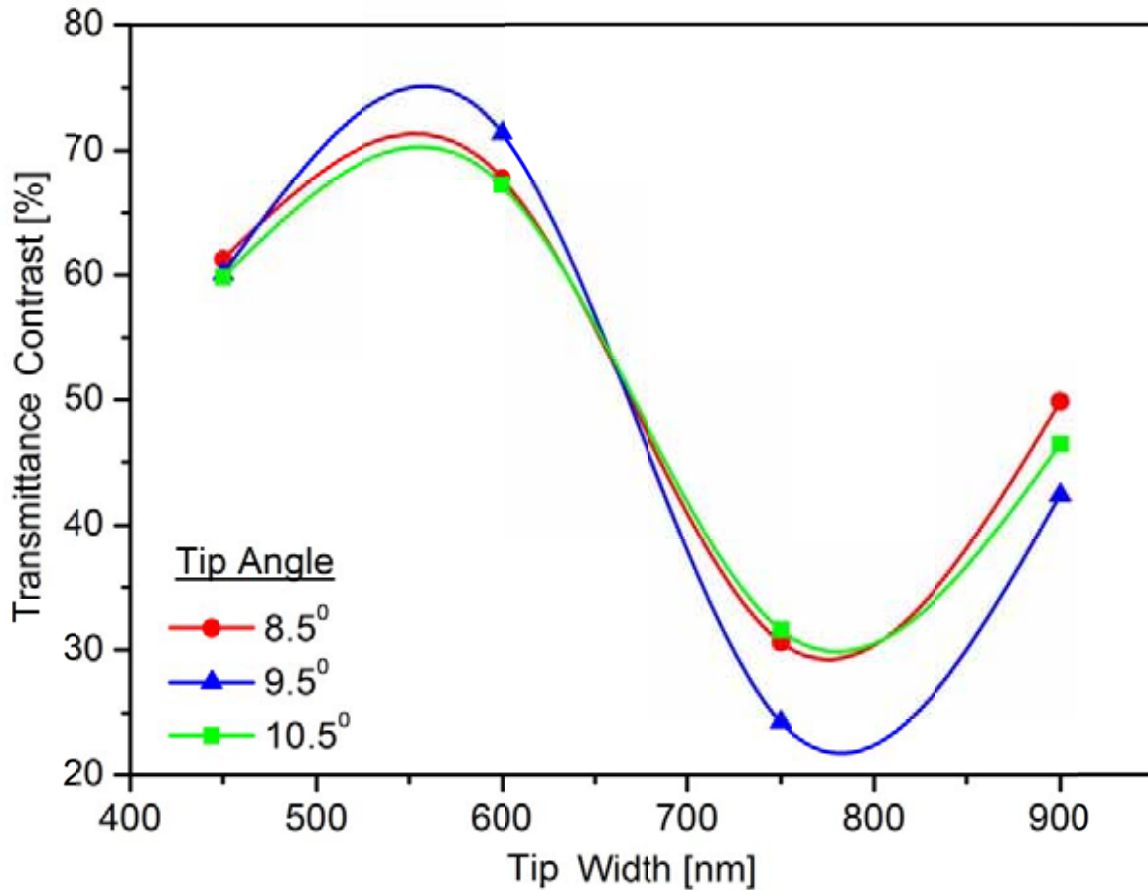

Figure 35: *Calculated transmittance at the tip angles, θ, of 8.5º, 9.5º and 10.5º for 450 nm, 600 nm, 750 nm and 900 nm tip widths.*

Results show that peak in transmittance contrast occurs at about 560 nm tip width in the three studied tip angles. The highest sensitivity, hence, at 560 nm tip width is calculated to be 1.01 nm per percent of light intensity when tip angle is 9.5º. Also, the minimum contrast takes place at 770 nm tip width again for 9.5º tip angle. The lowest sensitivity, at this point, is 3.40 nm per percent of light intensity. As aforementioned and it can be seen in Fig. 35, measurement sensitivities of TYPE 2 sensors can be determined in the design stage by proper selection of tip width and tip angle for constant tip-end size and thickness of 100 nm and 260 nm, respectively. Same approach illustrated herein can be applied for various tip-end sizes, tip angles and thicknesses to reach optimal tip width for the desired sensitivities and their applications.

Several models appropriate for short-range high-sensitivity TYPE 2 sensors are obtained. Studies proved that tip width, tip-end size, tip angle and thickness affect optical characteristics. Based on the efforts spent up to now at least three different sensor designs are understood to be very suitable for realization of the short-range sensors among other suitable designs when compared to those achieved in TYPE 1. Numerical studies on TYPE 2 sensors are still on the way for optimal solution, however, so far the highest sensitivity per percent of light intensity is calculated to be 0.97 nm at 9.5º tip angle for 100 nm tip-end size, 300 nm thickness and 600 nm tip width, and the lowest sensitivity is calculated to be 3.40 nm at 10.5º tip angle for 200 nm tip-end size, 170 nm thickness and 600 nm tip width. These sensitivities are numerically understood to be clearly superior over almost all possible designs reached in TYPE 1. The smallest and largest measurement ranges achievable are foreseen to be 97 nm and 330 nm, respectively.

3.2.3. Fabrication

TYPE 2 sensor is fabricated in order to understand characteristics and confirm results of the numerical study experimentally. Figure 36 illustrates SEM image of the fabricated sensor prior to device release by Vapor HF Etching. The sensor geometries are successfully etched into silicon down to SiO_2 layer. Tip angles are also manufactured precisely. Critical dimension at sensor springs and actuator fingers with 200 nm are properly fabricated as well. What in reality will be integrated into the applications is indeed only the region 50μm × 80μm in size.
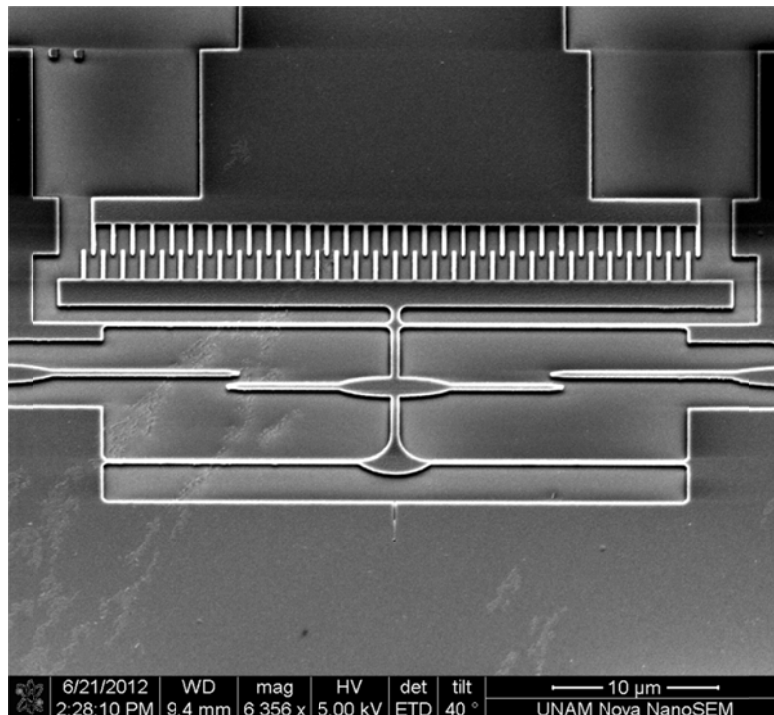

Figure 36: *SEM micrograph of the fabricated short-range high-sensitivity sensor.*

4. PHASE 3

In PHASE 1 and PHASE 2, displacement sensors with normally-off large-range low-sensitivity and short-range high-sensitivity characteristics are studied. In this phase, on the other hand, short-range high-sensitivity in-plane displacement sensors again, but at normally-on state are being investigated in order to clarify their initial state effects on the sensing characteristics. Towards this goal, three major types of sensor approaches are currently being investigated as presented below. All sensors utilized in PHASE 3 are based on Electromagnetic Field Modulation (EFM).

4.1. Normally-on Short-range High-sensitivity Physical Contact Displacement Sensor TYPE 1

The preliminary numerical studies as mentioned already in the project proposal regarding PHASE 2 were promising towards realization of short-range high-sensitivity displacement sensors. Hence, having completed TYPE 1 and TYPE 2 sensors of PHASE 2, the geometry as shown in Fig. 37 is deployed and investigated as PHASE 3, called as TYPE 1.

4.1.1. Sensor Principle

As shown in Fig. 37, the sensor structure is composed of one straight and half-circled waveguides. The list of parameters for such a sensor design includes radius of the circled waveguide, distance between the two waveguides, and device silicon thickness. The preliminary numerical study in FDTD analysis, for 500 nm waveguide width, 2 μm radius and 260 nm silicon thickness, for example, has shown 97.73% optical transmittance, an extinction down to 6.81% between 25 nm and 100 nm displacement values, respectively. This result suggests high-sensitivity measurement capability in short displacement ranges. An electrostatic comb drive similar to that discussed in PHASE 1 and PHASE 2 will be employed as the source of motion for changing distance, D, values to imitate real-life applications.
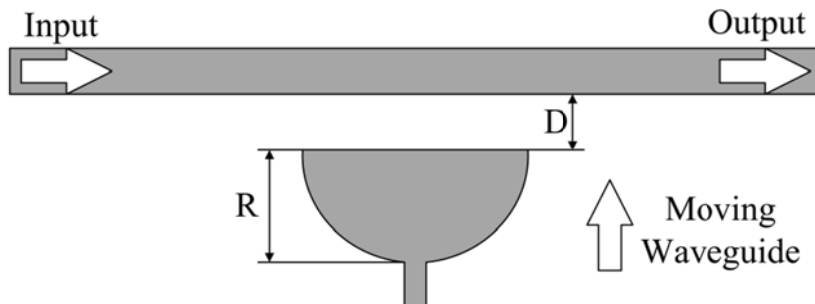

Figure 37: *Schematic view of TYPE 1 tip geometry for normally-on short-range high-sensitivity displacement sensing.*

4.1.2. Numerical Study in FDTD

Various radii of 0.5 μm, 1 μm, 2 μm, 4 μm, 6 μm, 8 μm, and 10 μm, at the distances of 0 nm, 25 nm, 50 nm, 75 nm, 100 nm, 300 nm, and 600 nm are simulated. Outcomes of the calculation in FDTD are provided and discussed in the following sections of this report.

4.1.2.1. Effect of Radius of Circled Waveguide

Optical performance of TYPE 1 sensor structure of this phase is studied at 25 nm, 50nm, 75nm, 100nm, 300nm and 600 nm distances, whose results are as shown in Figs. 38 and 39. First, effect of the radius of circled-waveguide at 2 μm, 3 μm, 4 μm, and 5 μm is investigated. Results are as provided in Fig. 38. Transmittance of such sensors is numerically observed to be significantly changing within sub-100nm distances. When radius of circled-waveguide decreases, sensivity of the sensor increases, however relative change between various circled-waveguides are not significantly large. Optical transmittance of the sensor when a radius of 2 μm, for example, is used in the circled-waveguide changes from 97.73% to 6.81% between 25 nm and 100 nm displacement values, respectively, corresponding to a sensitivity of about 0.83 nm per percent of light intensity.
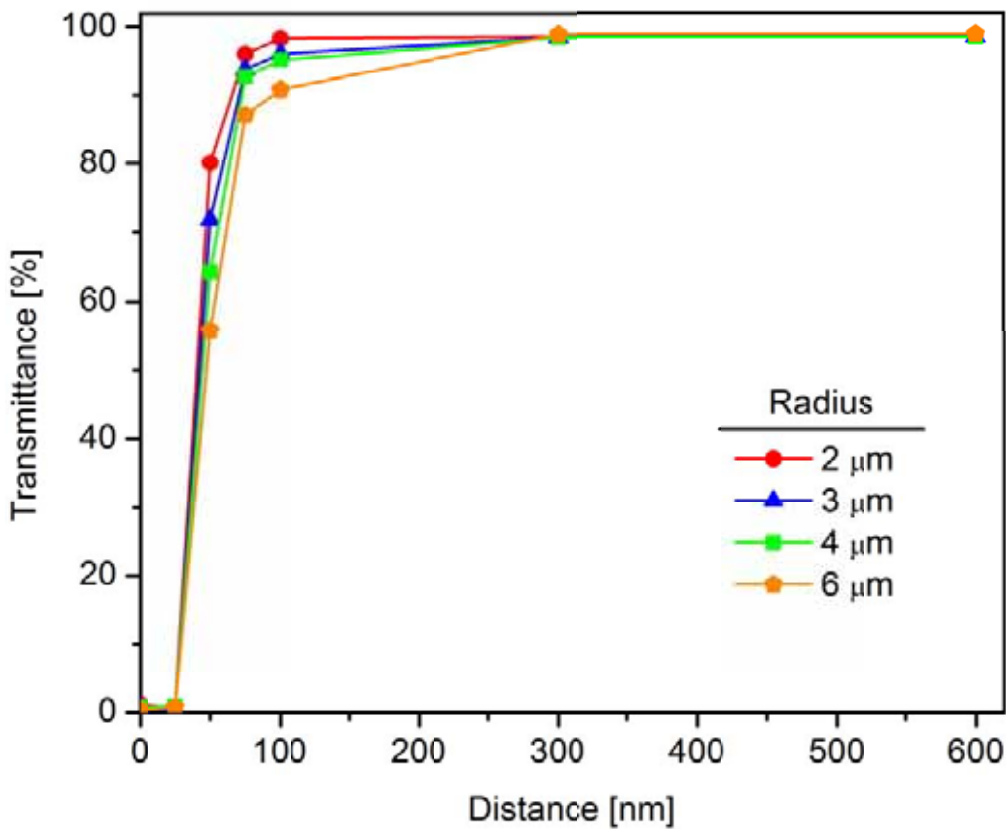

Figure 38: *Calculated transmittance at the circled-waveguide radii, R, of 2 μm, 3 μm, 4 μm, and 5 μm.*

After the effect of circled-waveguide radius on optical characteristic is understood, range of radii is enlarged for further clarification. Such radii, R, as 0.5 μm, 1 μm, 2 μm, 3 μm, 4 μm, 6 μm, 8 μm, and 10 μm for distances of 0 to 100 nm are studied, and the results are illustrated in Fig. 39. For all radii, high transmission contrast is obtained between distances, D, of 25 nm and 50 nm. Optimum radius towards short-range high-sensivity measurement is selected to be 2 μm. Optical performances for all studied sensors are showed that sensitivities around 1 nm are achievable as they have been aimed.
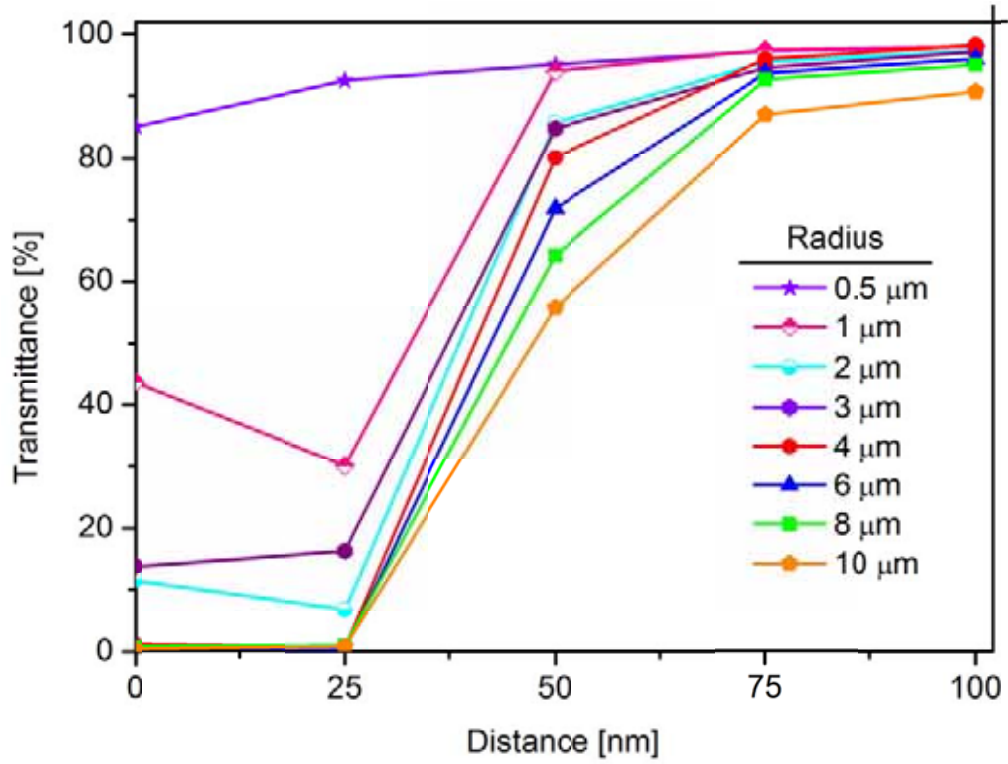
Figure 39: *Calculated transmittance at the circled-waveguide radii, R, of 0.5 μm, 1 μm, 2 μm, 3 μm, 4 μm, 6 μm, 8 μm, and 10 μm.*

4.2. Normally-on Short-range High-sensitivity Physical Contact Displacement Sensor TYPE 2

4.2.1. Sensor Principle

As shown in Fig. 40, the sensor structure is composed of a straight and triangle waveguides. The list of parameters for such a sensor design includes length of edge of the triangular-waveguide, a, distance between waveguides, D, and device silicon thickness. The preliminary numerical study in FDTD analysis for 500 nm waveguide width, 10 μm edge size, a, and 260 nm silicon thickness values, for example, has shown 60.11% optical transmittance, an extinction ratio down to 0.73% between 25 nm and 30 nm displacement values, D, respectively. Such a typical value suggests high-sensitivity measurement capability in short displacement ranges. An electrostatic comb drive similar to that discussed in PHASE 1 and PHASE 2, again, will be employed as the source of motion for changing distance, D, values to imitate real-life applications.
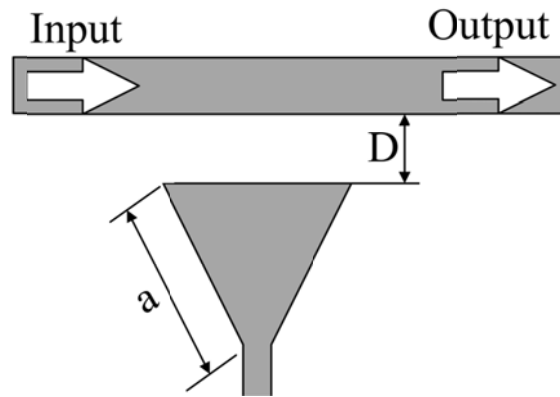

Figure 40: *Schematic view of TYPE 2 tip geometry for normally-on short-range high-sensitivity displacement sensing.*

4.2.2. Numerical Study in FDTD

Various triangular-waveguide edge sizes of 2 μm, 3 μm, 4 μm, 6 μm, 8 μm, and 10 μm, at the distances of 0 nm, 25 nm, 30 nm, 35 nm, 40 nm, 45 nm, 50 nm, 75 nm, 100 nm, 300 nm, and 600 nm are simulated. Outcomes of the calculation in FDTD are provided and discussed in detail below.

4.2.2.1. Effect of Edge Size of Triangular Waveguide

Optical performance of TYPE 2 sensor structure is studied at 0 nm, 25 nm, 30 nm, 35 nm, 40 nm, 45 nm, 50 nm, 75 nm, 100 nm, 300 nm, and 600 nm distances, for an edge length, a, 10 μm, whose results are shown in Fig. 41. Insets in Fig. 41 illustrate propagation of lightwave at the junction of the two waveguides. Optical performance for this sensor candidate with 10 μm edge of triangular-waveguide, for instance, is obtained to change from 0.73% to 60.11% between 25 nm and 30 nm displacement values, respectively, corresponding to a sensitivity of 0.084 nm per percent of light intensity.
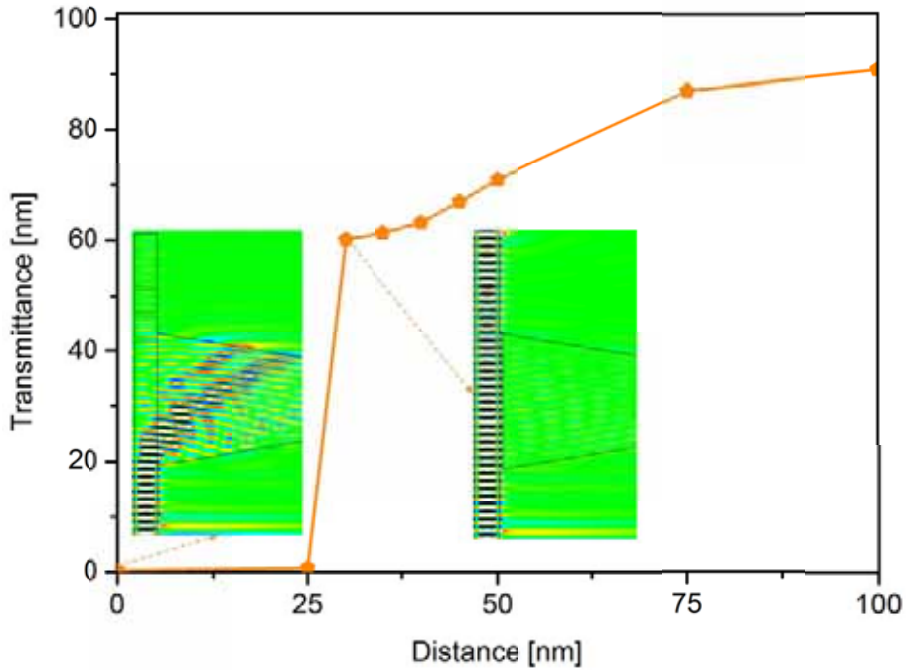
Figure 41: *Calculated transmittance for triangular-waveguide edge length, a, of 10 µm.*

After the effect of triangular-waveguide edge length on optical characteristic is understood, range of edge length, a, is enlarged for further clarification. Such lengths, a, as 2 µm, 3 µm, 4 µm, 6 µm, 8 µm, and 10 µm for distances from 0 to 100 nm are studied, and the results are illustrated in Fig. 42. For all edge lengths, high transmission contrast is obtained between distances, D, of 25 nm and 30 nm. As the size of triangular-waveguide's edge decreases, sensor's sensitivity increases. Maximum sensitivity, 0.064 nm per percent of light intensity, towards short-range high-sensitivity measurement in TYPE 2 sensors is selected to be at a of 2 µm. Optical performances for all studied sensors are showed that sensitivities around 1 nm are achievable as they have been aimed.
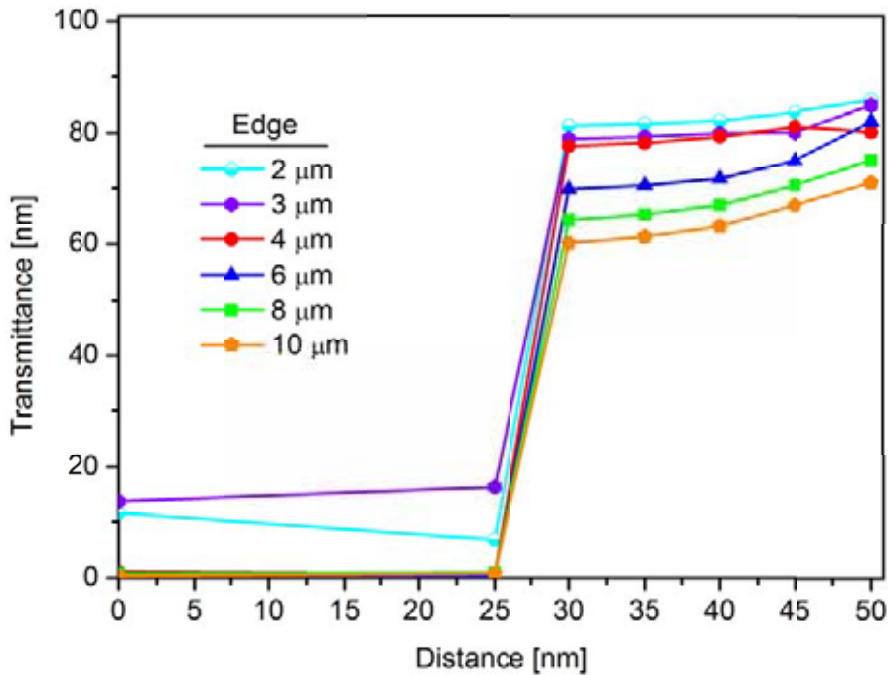

Figure 42: *Calculated transmittance at the triangular-waveguide edge length, a, of 2 µm, 3 µm, 4 µm, 6 µm, 8 µm, and 10 µm.*

4.3. Normally-on Short-range High-sensitivity Physical Contact Displacement Sensor TYPE 3

4.3.1. Sensor Principle

As shown in Fig. 43, the sensor structure is composed of a straight and a bent waveguides. The list of parameters for such a sensor design includes width of bent radius, distance between waveguides, contact length, and device silicon thickness. The preliminary numerical study in FDTD analysis, for 500 nm waveguide width, 40° bent waveguide and 260 nm device silicon thickness, and 4.8 μm contact length, for example, has shown 82.11% optical transmittance on the second waveguide at 0 nm, 84.27% optical transmittance on the first waveguide at 50 nm distance. Such a typical value suggests high-sensitivity measurement capability in short displacement ranges. An electrostatic comb drive similar to that discussed in PHASE 1 and PHASE 2, will be employed as the source of motion for changing distance, D, values to imitate real-life applications.
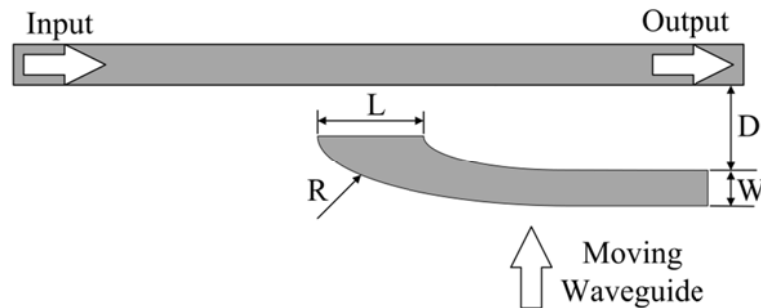

Figure 43: *Schematic view of TYPE 3 tip geometry for single-input two-output normally-on short-range high-sensitivity displacement sensing.*

4.3.2. Numerical Study in FDTD

At this stage, TYPE 3 sensor with the widths of the first and second waveguide as 500 nm, bent for the second waveguide of 40°, a contact length of 4.8 μm are simulated. The study included the distances, D, as 0 nm, 25 nm, 50 nm, and 100 nm. The outcome of the computational study is given in Fig. 44. Transmittance of this particular type of sensor changes significantly between 25 and 50 nm distances. While at distances below 25 nm, lightwave propagates through the second waveguide, above that of 50 nm, it propagates through the first one. Transmittance values at a distance of 0 nm on the first and the second waveguides are 0.12% and 82.11%, respectively, whereas those at a distance of 50 nm on the first and second waveguides are 84.27% and 2.43%, respectively. Hence, TYPE 3 sensors are seen to yield a sensitivity of about 0.30 nm per percent of light intensity.
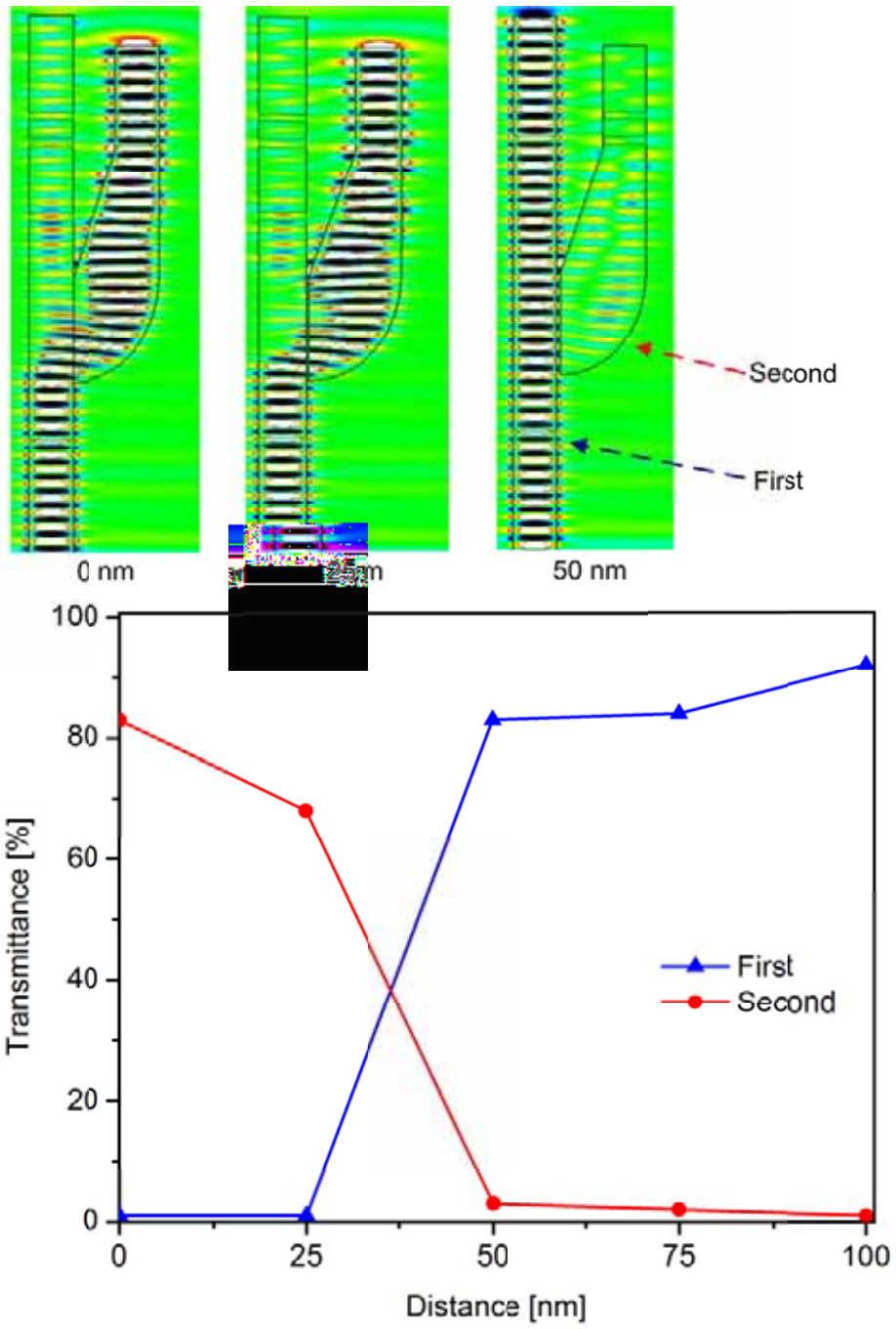
"NANO-DISP"

Figure 44: *Calculated transmittance for the widths of the first and second waveguide as 500 nm, a contact length of 4.8 μm.*

5. SUMMARY

The project is composed of four phases total. The first three are towards in-plane, whereas the last one is towards out-of-plane displacement/distance sensing. In the first two phases, PHASE 1 and PHASE 2, normally-off and in PHASE 3 normally-on sensors are investigated. While PHASE 1 focuses on large-range low-sensitivity sensors, PHASE 2 focuses on short-range high-sensitivity ones. This Periodic Report mentions numerous sensor designs obtained within the concept of the Project Proposal named "*NANO-DISP: Theoretical and Experimental Investigation of Synchronous Silicon Nanowire Waveguide Displacement Sensors*" towards large-range low-sensitivity and short-range high-sensitivity measurement characteristics as promised in PHASE 1 and PHASE 2, respectively, in the first 33 months of the project where change of institution takes place. 3D Finite-Difference Time-Domain (FDTD) Analysis is utilized in the efforts towards numerical characterization of the sensors. PHASE 1 involved a single type of sensing mechanism, whereas in PHASE 2, two types of mechanisms are considered. Three types of sensing mechanisms are introduced in PHASE 3.

Sensors in PHASE 1 are based on waveguide tips with elliptical geometry. Results demonstrated that the angle and length of tip geometry affect optical characteristics of the sensors under consideration. Among all suitable sensors, the highest sensitivity per percent of light intensity is calculated to be 5.74 nm at 80º tip angle for 4.8 μm tip length and 1.5 μm tip width, and the lowest sensitivity is calculated to be 9.62 nm at 85º tip angle for 12.0 μm tip length and 1.5 μm tip width. The smallest and largest measurement ranges achievable are foreseen to be 674 nm and 1062 nm, respectively.

First type of the sensors studied in PHASE 2 is based on waveguide tips with elliptical geometry similar to those in PHASE 1. The novelty for this type, however, is the use of tip angles below the Brewster's. Among all appropriate sensors in this type are those with 4.8 μm tip length and 1.5 μm tip width. The highest sensitivity is 1.10 nm per percent of light intensity at 10º tip angle, and the lowest sensitivity is 5.74 nm per percent of light intensity at 50º tip angle. The smallest and largest measurement ranges achievable based on calculations are predicted to be 135 nm and 674 nm, respectively. Second type of the sensors investigated in PHASE 2 is composed of two identical waveguides with tapered tips with abrupt ends. Studies proved that tip width, tip-end size, tip angle and thickness affect optical characteristics. Numerical studies on TYPE 2 sensors are still on the way for optimal solution, however, so far the highest sensitivity per percent of light intensity is calculated to be 0.97 nm at 9.5º tip angle for 100 nm tip-end size, 300 nm thickness and 600 nm tip width, and the lowest sensitivity is calculated to be 3.40 nm at 10.5º tip angle for 200 nm tip-end size, 170 nm thickness and 600 nm tip width. The smallest and largest measurement ranges achievable are calculated to be 97 nm and 330 nm, respectively.

In PHASE 3, short-range high-sensitivity in-plane displacement sensors again, but at normally-on state are being investigated in order to clarify their initial state effects on the sensing characteristics. Towards this goal, three major types of sensor approaches are studied. All sensors utilized in PHASE 3 are based on Electromagnetic Field Modulation (EFM). Sensitivities achieved in this phase are from 0.84 nm down to 0.06 nm per percent of light intensity within sub-100 nm distances.

Among major milestones succeeded in the project so far, procurement of two and three dimensional design and file conversion software for use in sensor design process, and FDTD Analysis software and the workstations for numerical studies can be counted. In addition, Micro/Nano Research Centers suitable for successful fabrication of the promised sensors are contacted and agreed. Fabrication of the sensor devices is being carried out at the agreed

cleanroom of Bilkent University, Ankara, Turkey's *National Nanotechnology Research Center* (*UNAM*, http://www.nano.org.tr/). Graduate student researchers are hired, educated and trained, and micro/nano-fabrication recipes are clarified after significant number of iterations. The project workpackages are completed and accomplished in the so-called *Nanophotonic Systems Research Laboratory* (*NANOPSYS*) mostly at Ozyegin University and the very small portion of the rest very recently at Istanbul Technical University (http://www.itu.edu.tr/), Istanbul, Turkey. *NANOPSYS* currently involves three graduate and two undergraduate students as well as the Principal Investigator (PI). Design and fabrication of home-made Vapor HF Etching Setup for Device Release is realized with the help of the undergraduate students. Finally, fund search for procurement of both Mechanical and Optical Sensor Characterization Setups, and their installation are completed. When compared to the project's workplan promised in the proposal, owing to the duration it took to grant the support for the procurement of characterization setups from a subsequent funding agency, *the Scientific and Technological Research Council of Turkey* (*TUBITAK*, http://www.tubitak.gov.tr/en/ot/10/), in addition to EC FP7 Marie Curie IRG Programme's Support, the project is delayed approximately by four to six months from the experimental point of view. However, the grant needed for the characterization setups are ensured properly, and as a result, currently, both mechanical and optical characterization of the sensors promised at PHASE 1 are very close to the end, predicted to be completed in a month. Because of the delay in granting subsequent funding, it hasn't been possible for the research group to fulfill and include the experimental characterization results into this report at hand unfortunately. Nevertheless, in order to make the delay up and to ensure completion of the promised workpackages fully in the rest of the project's total duration of four years, the research group had already gone ahead to the second phase, PHASE 2, and third phase, PHASE 3, and completed more than that planned in terms of numerical analysis and design. As a result, we anticipate that all workpackages will be fulfilled prior to the end of the project term successfully. Despite difficulties encountered, PI has succeeded to reach the critical mass within the European Union in financial, infrastructural and researcher aspects in order to ensure microfabrication and characterization of high-sensitivity embedded optical displacement/distance sensors.

6. REFERENCES

[1] E. Bulgan, Y. Kanamori, and K. Hane, "*Connection characteristics of silicon nanowire waveguides and fabrication of physical contact switches,*" 15th Int'l Conference on Solid-State Sensors, Actuators and Microsystems (IEEE Transducers), Colorado, USA, pp.505-508, (2009).

[2] B. Jalali and S. Fathpour, "*Silicon Photonics,*" J. Lightwave Technol., vol. 24, pp.4600-4615, (2006).

[3] T. Hirano, T. Furuhata, K.J. Gabriel, and H. Fujita, "*Design, fabrication and operation of sub-micron gap electrostatic comb-drive actuators,*" J. Microelectromech. S., vol. 1, pp.52-59, (1992).

[4] D.J. Monk and D.S. Soane, "*Determination of the etching kinetics for the hydrofluoric acid/silicon dioxide system,*" J. Electrochem. Soc., vol. 140, pp.2339-2346, (1993).

[5] A. Witvrouw, B.D. Bois, P.D. Moor, A. Verbist, C.A. Van Hoof, H. Bender, and C. Baert, "*A comparison between wet HF etching and vapor HF etching for sacrificial oxide removal,*" Proceedings of SPIE: Micromachining and Microfabrication Process Technology VI, vol. 4174, SPIE, Santa Clara, USA, pp.130-141, (2000).